

TRIANNUAL REPORT

on the

DESIGN, ANALYSIS AND TEST VERIFICATION  
OF ADVANCED ENCAPSULATION SYSTEMS

For Period Ending

March 31, 1984

Contract 055567

6321-52

Prepared by:

Alexander Garcia III

Approved by:

  
\_\_\_\_\_  
Nick Mardesich  
Manager, Advanced Programs

SPECTROLAB, INC.  
12500 Gladstone Avenue  
Sylmar, California 91342

August 1984

The JPL Flat-Plate Solar Array Project is sponsored by the U.S. Department of Energy and forms part of the Solar Photovoltaic Conversion Program to initiate a major effort toward the development of low cost solar arrays. This work was performed for the Jet Propulsion Laboratory, California Institute of Technology by agreement between NASA and DOE.

This report was prepared as an account of work sponsored by the United States Government. Neither the United States nor the United States Department of Energy, nor any of their employees, nor any of their contractors, subcontractors, or their employees, makes any warranty, express or implied, or assumes any legal usefulness of any information, apparatus, product or process disclosed, or represents that its use would not infringe privately-owned rights.

## TABLE OF CONTENTS

<u>Section</u>	<u>Title</u>	<u>Page</u>
1.0	SUMMARY .....	1
2.0	INTRODUCTION .....	2
3.0	TECHNICAL DISCUSSION .....	4
3.1	Transparent Conductive Polymers .....	4
3.2	Photovoltaic Specialists Conference Partici- pation .....	7
3.3	Wrap-Up of Phase III .....	7
	Appendix A - Electrical Isolation Analysis Phase 3C .....	11
	Appendix B - Structural Analysis Phase 3C .....	52

## Section 1.0

### SUMMARY

---

Investigations into transparent conductive polymers were begun. Polypyrrole was electrochemically deposited, but the film characteristics were poor. A proprietary polymer material supplied by Polaroid was evaluated and showed promise as a readily processable material.



## Section 2.0

### INTRODUCTION

---

This program will develop the analytical methodology for advanced encapsulation designs. From these methods design sensitivities will be established for the development of photovoltaic module criteria and the definition of needed research tasks.

The program consists of four phases. In Phase I analytical models were developed to perform optical, thermal, electrical and structural analyses on candidate encapsulation systems. From these analyses several candidate encapsulation systems were selected for qualification testing during Phase II. Additionally, during Phase II, test specimens of various types will be constructed and tested to determine the validity of the analysis methodology developed in Phase I.

During Phase III the following items will be covered:

1. Correction of identified deficiencies and/or discrepancies between analytical models developed during Phase I and relevant test data obtained during Phase II of the above contract.
2. Improvement and extension of prediction capability of present analytical models.
3. Generation of encapsulation engineering generalities, principles, and, design aids for photovoltaic module design.

From these items the sensitivity of module performance to various material properties will be determined. This study will enable the intelligent direction of research into assessment of module life potential by analyzing those materials and their properties which through aging would most influence module performance.

In Phase IV a final optimum design based on knowledge gained in Phases I, II and III will be developed and delivered to JPL.

## Section 3.0

### TECHNICAL DISCUSSION

---

#### 3.1 Transparent Conductive Polymers

The equipment for the electrochemical deposition of polymeric films has been received and set up. Preliminary experimentation was begun using pyrrole in an acetonitrile solution with 0.1 M electrolyte. The electrolyte initially used was tetraethylammonium tetrafluoroborate. Films were deposited in ITO coated glass slides which had been masked with tape to leave a 1.0 x 1.0 deposition area.

These initial experiments yielded poor quality films. Deposition of the films began at edges and corners, but did not cover the entire area.

SEM micrographs were taken of polypyrrole films grown on indium tin oxide coated glass slides. Figures 1, 2, and 3 show typical films. The films start depositing at several nuclei and then slowly grow outward. The nuclei grow slightly in area and then become thicker, rather than growing in area. Figure 1 shows two areas (finger-like areas left of center) which are typical. Higher magnifications show a highly textured surface. Changing the deposition rate did not improve the character of the films. To provide a better nucleation site on the substrate surface, glass slides were prepared with a thin evaporated coating

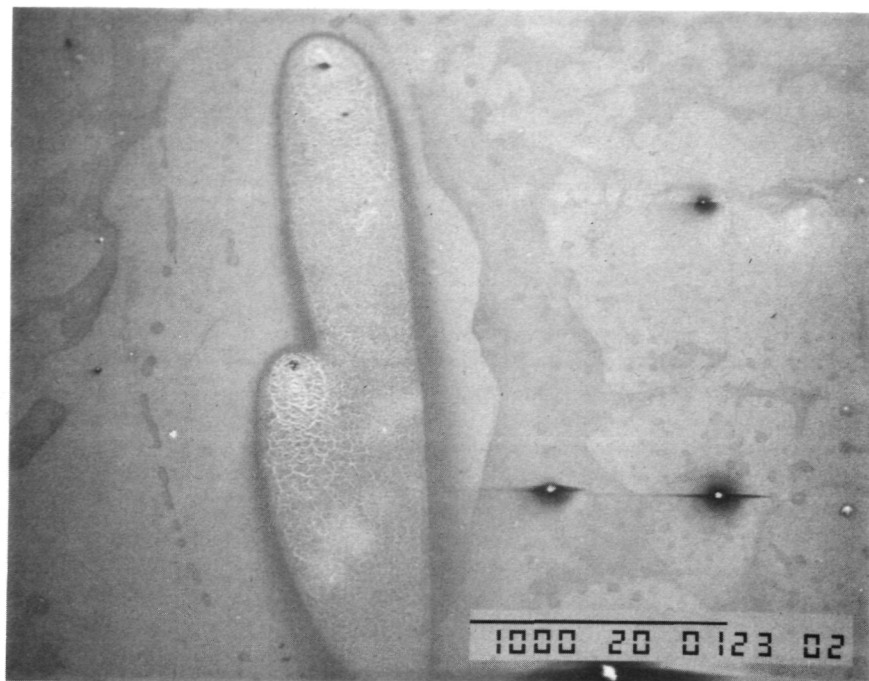


Figure 1. POLYPYRROLE ON ITO 35X

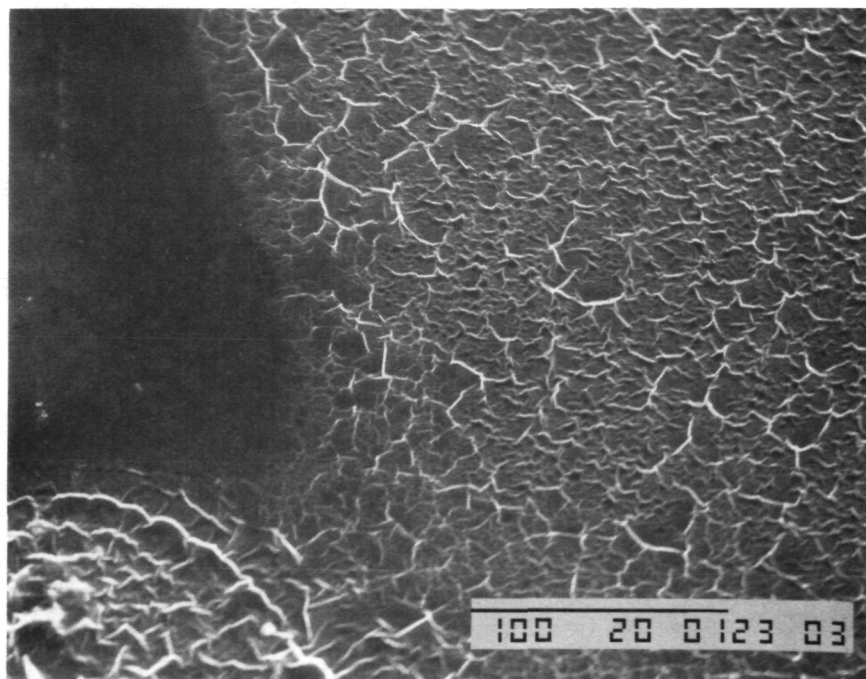


Figure 2. POLYPYRROLE ON ITO 350X

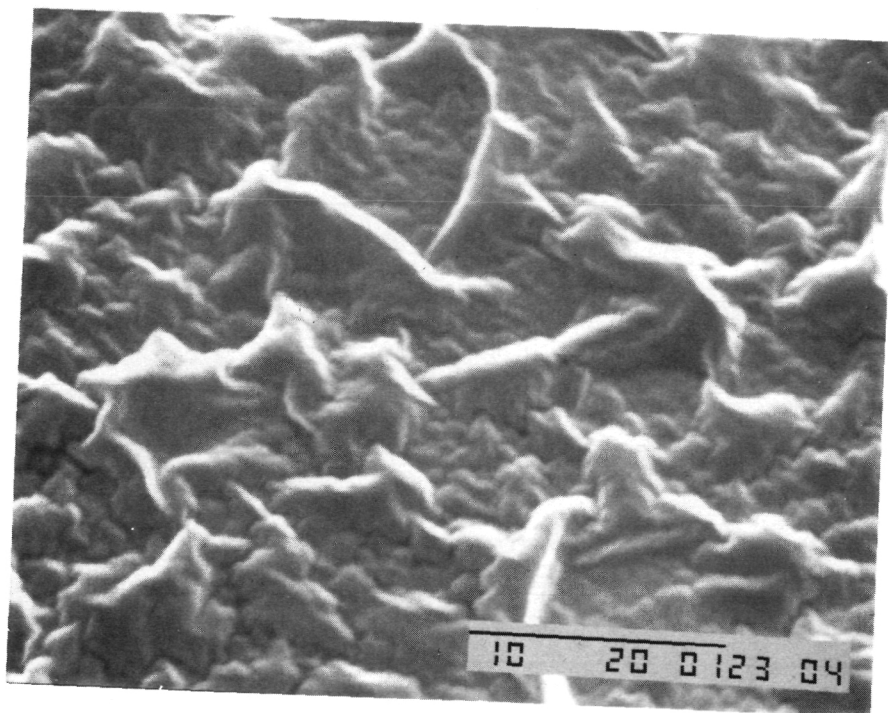


Figure 3. POLYPYRROLE ON ITO 3500X

of palladium. Figures 4, 5, and 6 show a typical film prepared on this substrate. Nucleation sites were much closer but the film still had a rough texture. Microscopically the sample showed great nonuniformity and none of the samples were suitable for characterization.

Preliminary experiments with a conductive polymer supplied by Polaroid were encouraging. The proprietary material was spun onto several cells and showed good antireflection properties. Electrical properties were not measured. An agreement between Spectrolab and Polaroid will be necessary to continue work on this material. This is the first conducting polymer which is available to be used directly by a spin coating technique.

### 3.2 Photovoltaic Specialists Conference Participation

Two papers were accepted for presentation at the 16th IEEE Photovoltaic Specialists Conference in Orlando, Florida.

### 3.3 Wrap-Up of Phase III

Work has been completed on the additional electrical and structural tasks. Two reports are included as appendices to this document. This work completes the experimental portion of Phase III of this Contract. A final report including Phases I-IV will be issued in the fall.

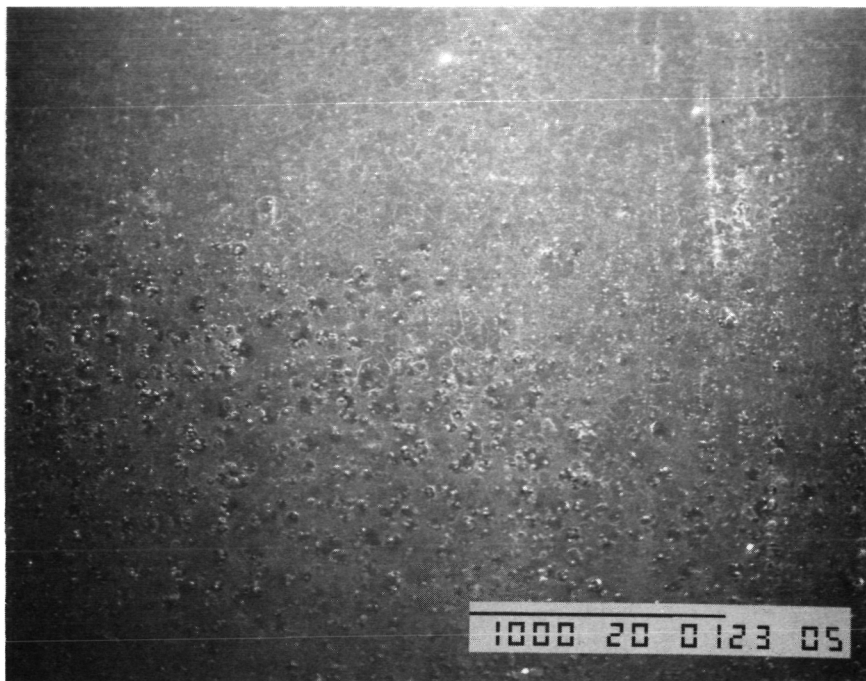


Figure 4. POLYPYRROLE ON PALLADIUM 35X

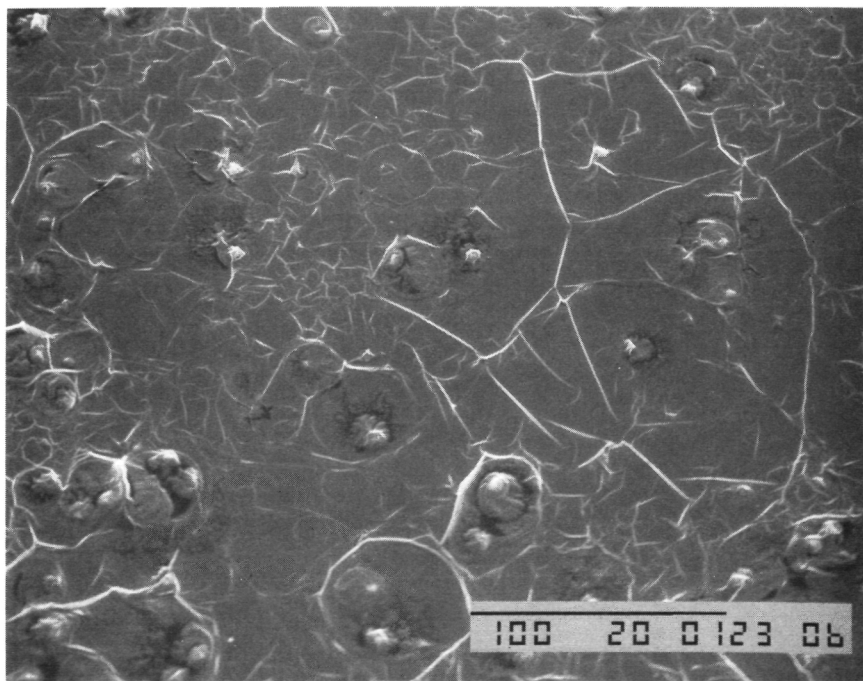


Figure 5. POLYPYRROLE ON PALLADIUM 350X

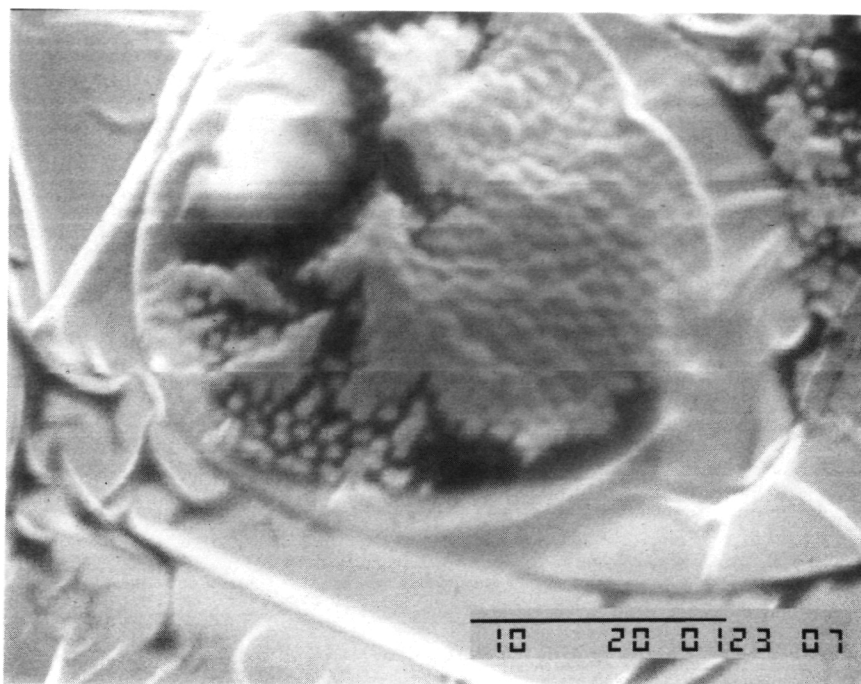


Figure 6. POLYPYRROLE ON PALLADIUM 3500X



#### Section 4.0

##### CONCLUSIONS AND RECOMMENDATIONS

---

There are no conclusions and recommendations for this period.

#### Section 5.0

##### PLANNED ACTIVITIES

---

During the next period Spectrolab will continue investigations into the electrochemical deposition of transparent conductive materials. The preparation of the final report on Phases I-IV will begin.

Report No. FR-84-72-606

HAC Ref. No. E4677

APPENDIX A

ELECTRICAL ISOLATION ANALYSIS

PHASE 3C

James M. Kallis, D. Charles Trucker, and Roque K. Szeto  
Hughes Aircraft Company  
El Segundo, California

March 1984

Submitted to Spectrolab, Inc., to document part of the work  
performed on "Design, Analysis, and Test Verification of  
Advanced Encapsulation Systems."

Spectrolab Contract No. 88774

a subcontract of

Jet Propulsion Laboratory Contract No. 955567

## TABLE OF CONTENTS

1.0	Introduction .....	16
1.1	Background .....	16
1.2	Present Investigation .....	17
2.0	Generalization and Extension of Electrical Stress Intensification Calculations ..	19
2.1	Approach .....	19
2.2	Thick-Cell Limit .....	19
2.3	Effects of Cell Edge Shape .....	22
2.4	Master Curve for Semicircular-edged Cell .....	23
2.5	General Master-Curve Formulas .....	23
2.6	Location of Maximum Electric Field .....	27
2.7	Application of Results to Design of Photovoltaic Modules .....	28
2.8	Area for Further Investigation .....	29
3.0	Calculation of Lines of Force of Three-Dimensional Electric Fields .....	30
3.1	Introduction .....	30
3.2	Basic Equations .....	30
3.3	Numerical Method for Lines of Force on Planes of Symmetry .....	33
3.4	Lines of Force for the Electrochemical Corrosion Test Geometry .....	42
4.0	Conclusions .....	49
5.0	Recommendation .....	50
	Acknowledgements .....	50
	References .....	50

## LIST OF ILLUSTRATIONS

Figure	Page
1-1 Electrical Analysis Objective .....	16
1-2 Disc-shaped Solar Cell .....	17
1-3 Geometric Limits For Which the Finite-Element Model Incurs Numerical Difficulties .....	18
2-1 Configuration of Thick-Cell Limit ( $t_p/t_c \rightarrow 0$ ) .....	20
2-2 Solution For Infinitely Thick Cell .....	21
2-3 Shapes of Curves For Fixed $t_p/R$ .....	23
2-4 Shape of Curve For Semicircular Edge .....	24
2-5 Shapes of Master Curves .....	24
2-6 Shapes of Curves For Fixed $t_p/t_c$ .....	25
2-7 Master Curves for Electrical Stress Intensification .....	26
2-8 Location of Maximum Electric Field .....	27
2-9 Location of Maximum Electric Field on Semicircular-edged Cell— Thin-cell Limit .....	28
3-1 Lines of Force and Stream Functions .....	31
3-2 Equipotentials and Lines of Force for Circular Potentials of Example 1 .....	38
3-3 Equipotentials and Lines of Force for Example 2 .....	39
3-4 Electrochemical Corrosion Test Specimen Geometry .....	43
3-5 ABCDEFG Plane—Qualitative .....	44
3-6 ABCDEFG Plane—Quantitative (Near AB) .....	45
3-7 ABCDEFG Plane—Quantitative (Far from AB) .....	46
3-8 AHIIKB Plane—Qualitative .....	47
3-9 AHIIKB Plane—Quantitative .....	48

## LIST OF TABLES

Table	Page
3-1    The Exact $\phi$ ; $\psi$ and $p(x, y)$ Computed from Algorithm .....	40
3-2    Partial Derivatives Computed Using Cubic Splines, and the Residuals $\equiv \phi_x \psi_x + \phi_y \psi_y$ .....	41

## SUMMARY

A method was developed for calculating the magnitude and location of the maximum electric field for a family of solar-cell-like shapes. Simple formulas for use by photovoltaic module designers were developed. They provide quantitative information on the effects of the cell shape, cell thickness, and pottant thickness on the electrical stress intensification at the cell edge. It is recommended that a mathematical investigation be performed to verify what the design guidelines for advanced thin-film modules should be.

A method for calculating the lines of force for three-dimensional electric fields was developed and applied to a geometry of interest to the photovoltaic program.

## 1.0 INTRODUCTION

### 1.1 BACKGROUND

This report documents the latest in a series of investigations of the electrical isolation design of a photovoltaic module. The objective, as shown in Figure 1-1, is to provide guidance on how to design the module to prevent breakdown. The onset of breakdown can be expected at the location of the maximum electric field, which occurs at the edge or corner of a high-voltage cell. Accordingly, the effects of the cell edge/corner radius, the pottant thickness, and the cell thickness on the maximum electric field were investigated.

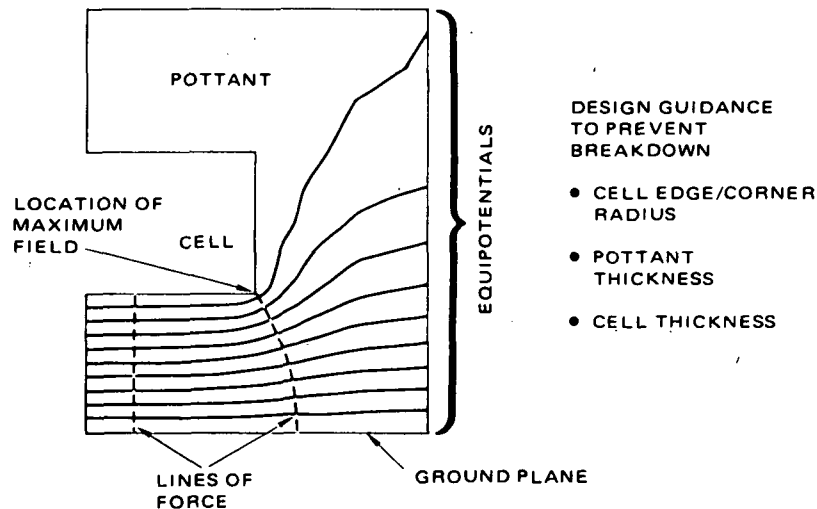


Figure 1-1. Electrical analysis objective.

In the first two phases of the investigation, one-dimensional analyses were performed (Ref. 1), and the breakdown voltages of typical module configurations were measured (Ref. 2). The thrust of the electrical isolation analysis performed in the third phase of the encapsulation contract was to develop a method of evaluating the multidimensional effects of

the module conductor geometry on the electric field, that is, the electrical stress intensification at edges and corners of the solar cells (Ref. 3). The multidimensional electric field was calculated with the finite-element-based NASTRAN Thermal Analyzer, using the analogy between thermal and electrostatic fields. To evaluate the maximum electric field accurately, the NASTRAN output had to be post-processed; a polynomial was fit to the predicted values of potential as a function of distance from the cell surface by the method of least squares, and the surface field was calculated from the best-fit polynomial. The accuracy of this method was verified by comparison with an exact solution for a geometry similar to that of typical solar cells. Two sample geometries were analyzed—a square test coupon used in electrical isolation tests performed earlier in this contract and a family of disc-shaped solar cells shown in Figure 1-2. In the figure,  $R$  = cell edge radius of curvature,  $t_c$  = cell thickness, and  $t_p$  = pottant

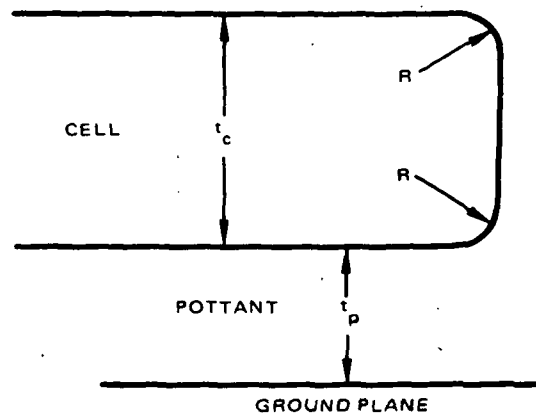


Figure 1-2. Disc-shaped solar cell.

thickness. These sample analyses demonstrated that this finite-element method is a useful design tool for evaluating candidate module encapsulation designs. They also showed geometric limits for which the model incurs numerical difficulties: 1) cells having very sharp edges (see Figure 1-3a), 2) cells much thinner than the dielectric pottant layer (Figure 1-3b), and 3) cells much thicker than the dielectric pottant layer (Figure 1-3c).

## 1.2 PRESENT INVESTIGATION

The present investigation consisted of the following tasks:

1. The previous work was extended to the limits for which the aforementioned multidimensional model encounters numerical difficulties. This analysis is described in Section 2.
2. A method was developed for calculating lines of force of three-dimensional electric fields for geometries relevant to photovoltaic modules. This method is described in Section 3.

Conclusions and recommendations are presented in Sections 4 and 5, respectively.





a. Sharp-edged cell:  $t_p/R \gg 1$ .



b. Thin cell or thick potant:  $t_p/t_c \gg 1$ .



c. Blunt-edged cell or thin potant:  $t_p/R \ll 1$ .

Figure 1-3. Geometric limits for which the finite-element model incurs numerical difficulties.

## 2.0 GENERALIZATION AND EXTENSION OF ELECTRICAL STRESS INTENSIFICATION CALCULATIONS

### 2.1 APPROACH

The generalized, extended calculations of the electrical stress intensification were obtained by an evolutionary process. The key elements were exact solutions for limiting cases, physical reasoning, and observing the behavior of the finite-element results when plotted in certain ways.

As in Ref. 3, we evaluate the results in terms of the dimensionless electrical stress intensification factor  $y$ , defined by

$$y = \frac{E_{pp}}{E_m} = \frac{V_0/t_p}{E_m}, \quad (2-1)$$

where

$E_{pp}$  = field for infinite parallel plates

=  $V_0/t_p$ ,

$V_0$  = voltage difference between solar cell and ground plane, and

$E_m$  = maximum electric field.

(In Ref. 4,  $y$  is denoted by  $\eta$  and is called the utilization factor. In Ref. 5,  $y$  is denoted by  $\eta$  and is called the efficiency factor.)

The cell shown in Figure 1-2 represents equally well a disc-shaped cell or the edge of a rectangular cell. It was found advantageous herein to consider the geometry to be two-dimensional planar. This simplified the finite-element analysis and enabled the method of conformal mapping to be used.

### 2.2 THICK-CELL LIMIT

The first step in the process was the discovery of an exact solution for the thick-cell limit, that is, the geometry shown in Figure 2-1. This solution was obtained by Dreyfus (Ref. 6) using conformal mapping.

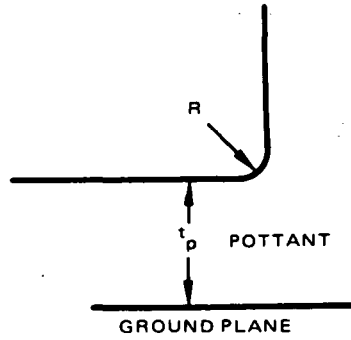


Figure 2-1. Configuration of thick-cell limit ( $t_p/t_c \rightarrow 0$ ).

The edge shape for which Dreyfus obtained the solution is not exactly a quarter circle. It is, however, very nearly a quarter circle, and the difference is insignificant for our purpose.

The solution is given in Equations (24) and (27) of Ref. 6. Equation (27) has a typographical error: a parameter " $\alpha$ " is typed as " $a$ ". In our notation, the correct equations are

$$\frac{1}{y} = \frac{(1 + S^2)^{1/2}}{S} \left[ \frac{\operatorname{arcsinh} S - \frac{S}{(1 + S^2)^{1/2}}}{S - \arctan S} + 1 \right], \quad \left( \frac{t_p}{t_c} \rightarrow 0 \right) \quad (2-2)$$

where  $S$  is related to  $t_p/R$  by

$$\frac{2}{\pi} \frac{t_p}{R} = \frac{1}{S - \arctan S} + \frac{1}{\operatorname{arcsinh} S - \frac{S}{(1 + S^2)^{1/2}}} \quad (2-3)$$

Because of the complexity of Equations (2-2) and (2-3), it is difficult to determine the asymptotic behavior as the edge becomes very blunt ( $t_p/R \rightarrow 0$ ) or very sharp ( $t_p/R \rightarrow \infty$ ). Therefore we evaluated the mathematical limits of the terms in these equations and obtained the following asymptotic formulas:

$$\frac{1}{y} \rightarrow 1 + 2 \frac{\pi R}{2 t_p} \exp\left(-\frac{\pi R}{2 t_p}\right) \text{ as } t_p/R \rightarrow 0, \quad (2-4)$$

$$\frac{1}{y} \rightarrow \frac{2}{(3\pi)^{1/3}} \left(\frac{t_p}{R}\right)^{1/3} = 0.9468 \left(\frac{t_p}{R}\right)^{1/3} \text{ as } t_p/R \rightarrow \infty. \quad (2-5)$$

The solution is plotted on log-log paper as  $y$  versus  $1 + (t_p/R)$  in Figure 2-2; in this form, the ordinate varies between 0 and 1. (The solution is plotted incorrectly in Refs. 4 and 5.)

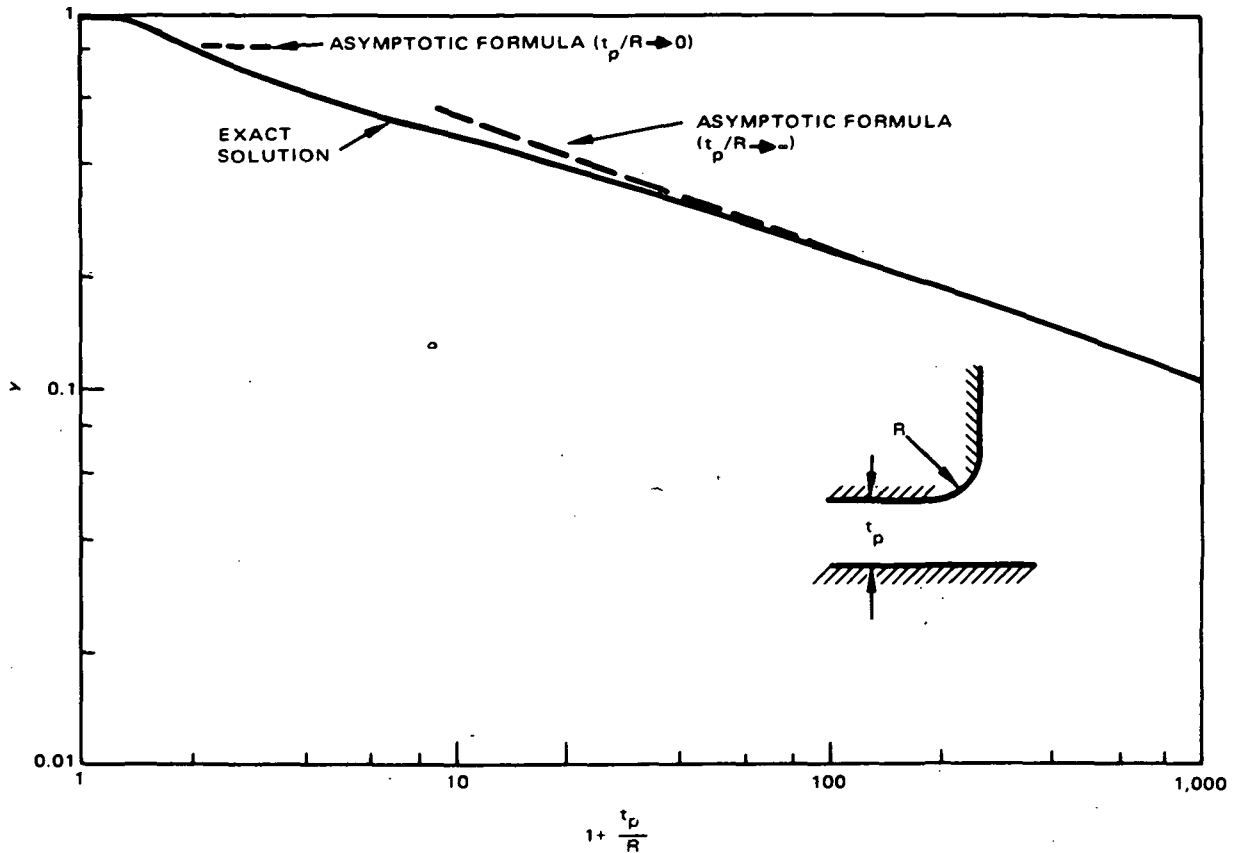


Figure 2-2. Solution for infinitely thick cell.

The asymptotic formula (2-4) is accurate to within 2 percent for  $t_p/R < 1$ . The asymptotic formula (2-5) is accurate to within 2 percent for  $t_p/R > 120$ . Therefore these simple asymptotic formulas can be used instead of the complicated Equations (2-2) and (2-3) for large ranges of the parameter  $t_p/R$ . We obtained an even simpler formula by observing that the complicated curve in Figure 2-1 is very nearly a straight line for  $t_p/R > 1$ ; this can be verified by placing a transparent straightedge over the curve. We thus found that the exact solution can be approximated by

$$\frac{1}{y} \approx \left(1 + \frac{t_p}{R}\right)^{0.325} \quad (2-6)$$

which is accurate to within 4 percent for  $1 \leq t_p/R \leq 120$ . Thus one can use either the exact Equations (2-2) and (2-3), the asymptotic formulas (2-4) or (2-5), or the approximate formula (2-6), depending on the purpose and the required accuracy.

The importance to the present analysis of the Dreyfus solution was as follows. It provided a basis for extrapolating and checking the finite-element results. It is often difficult to determine whether a numerical solution is accurate. We suspected that the finite-element results became inaccurate as the cell became thin or thick or as the edge became sharp, but it was difficult to evaluate where or by how much the numerical solution became inaccurate.

Thus the knowledge that the finite-element results must approach the Dreyfus solution in the limit as  $t_p/t_c \rightarrow 0$  was very valuable. The parameter grouping  $1 + (t_p/R)$  for plotting the Dreyfus solution, which is given in Ref. 4, and the shape of the curve in Figure 2-2 provided clues to what parameter groupings and what shapes of master curves would generalize and correlate the finite-element results. Furthermore, the Dreyfus solution provides a mathematical proof that  $y \rightarrow 0$  as  $t_p/R \rightarrow \infty$ ; we suspected this result on physical grounds but had encountered numerical difficulties in establishing this result with the finite-element method. This result means that  $y \rightarrow 0$  and  $E_m \rightarrow \infty$  as  $R \rightarrow 0$ . That is, for a fixed pottant thickness, the electric field approaches infinity as the edge of the high-voltage electrode (solar cell) becomes sharper; this result is well known to high-voltage equipment designers. It also means that  $y \rightarrow 0$  as  $t_p \rightarrow \infty$  (holding  $t_p/t_c$  fixed at a very small value). That is, for a fixed solar cell edge radius of curvature, the edge behaves increasingly like a perfectly sharp edge as the cell is moved further from the ground plane. In this limit, however, the maximum electric field decreases as the pottant thickness increases, because  $y$  varies as a fractional power of  $t_p$ ; from Equations (2-1) and (2-5), we have

$$\begin{aligned} E_m &= \frac{V_0}{t_p y} \rightarrow \frac{V_0}{t_p} 0.9468 \left( \frac{t_p}{R} \right)^{1/3} \\ &= 0.9468 \frac{V_0}{R} \left( \frac{t_p}{R} \right)^{-2/3} \rightarrow 0 \text{ as } t_p/R \rightarrow \infty, \text{ holding } R \text{ fixed.} \end{aligned} \quad (2-7)$$

### 2.3 EFFECTS OF CELL EDGE SHAPE

The effects of the cell edge shape were deduced by physical reasoning, along with an examination of the finite-element results and Dreyfus' limiting solution. We considered the family of geometries having a fixed value of  $t_p/R$ . The value of  $y$  is then a function of the parameter  $R/t_c$ , which can have values between 0 and 0.5. The limit  $R/t_c \rightarrow 0$  is the thick-cell limit for which the Dreyfus solution, described in Section 2.2, applies. The value 0.5 corresponds to a cell having a semicircular edge. Intermediate values of  $R/t_c$  correspond to cells having an edge with a flat portion.

By physical reasoning, we concluded that the value of  $y$  must be the highest for the Dreyfus limit and must decrease as  $R/t_c$  increases. This behavior occurs because the sun-side edge of the cell (the edge away from the ground plane) approaches the shade-side edge (where the maximum electric field occurs) as  $R/t_c$  increases, causing the lines of force to crowd together. In other words, the sun-side edge influences the shade-side edge, thus increasing the maximum electric field, as  $R/t_c$  increases. Therefore a plot of  $y$  versus  $1 + (t_p/t_c)$ , holding  $t_p/R$  fixed, must have the shape shown in Figure 2-3. The finite-element results were consistent with this shape. Furthermore, physical reasoning indicated that the slope of such a

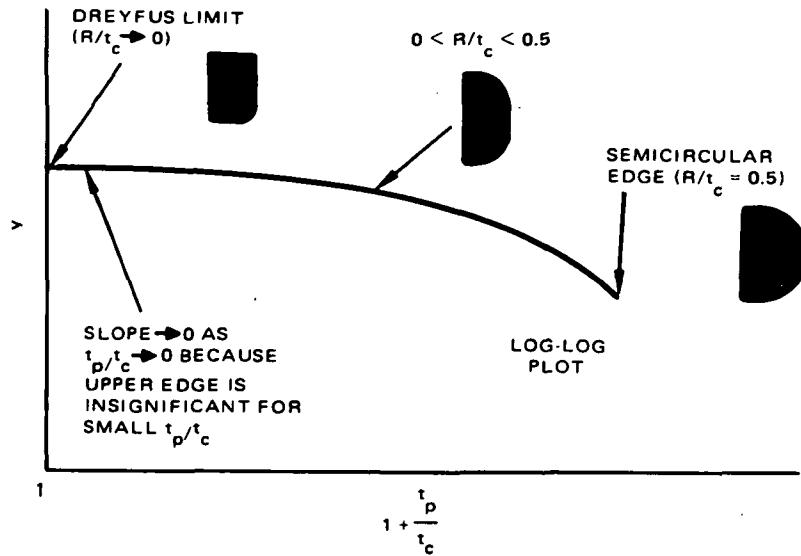


Figure 2-3. Shapes of curves for fixed  $t_p/R$ .

curve must approach zero as the Dreyfus limit is approached, because the effect of the sun-side edge is significant only for relatively large values of  $R/t_c$ . This behavior also was noted in the finite-element results.

This curve provided a check on the finite-element results. The numerical error inherently underestimated the maximum electric field and thus overestimated  $y$ . Once we realized what the shape of the curve in Figure 2-3 is, we were sure that any value of  $y$  predicted by the finite-element method was wrong if it was higher than the Dreyfus value for the same value of  $t_p/R$ . We discarded these obviously wrong predicted values from the presented data.

#### 2.4 MASTER CURVE FOR SEMICIRCULAR-EDGED CELL

Cuddihy (Ref. 7) noted that the finite-element results for the semicircular-edged cell gave very nearly a straight line with a slope of  $-0.5$  when plotted on log-log paper in the form  $y$  versus  $1 + (t_p/t_c)$ , as shown in Figure 2-4. Thus the following simple formula was obtained:

$$y \approx \left(1 + \frac{t_p}{t_c}\right)^{-1/2}, \text{ for } R/t_c = 0.5 \text{ and } 0.25 \leq t_p/t_c \leq 100. \quad (2-8)$$

This formula has no physical basis. However, it fits the finite-element calculations very closely, and it is consistent with power-law formulas obtained analytically for other geometries (see Equation (2-5) of this report and Ref. 7).

#### 2.5 GENERAL MASTER-CURVE FORMULAS

By combining the results of Sections 2.3 and 2.4, we deduced that the shapes of the curves in a log-log plot of  $y$  versus  $1 + (t_p/t_c)$  must be as shown in Figure 2-5. For fixed values of  $t_p/R$ , each curve has the shape shown previously in Figure 2-3 and approaches the straight

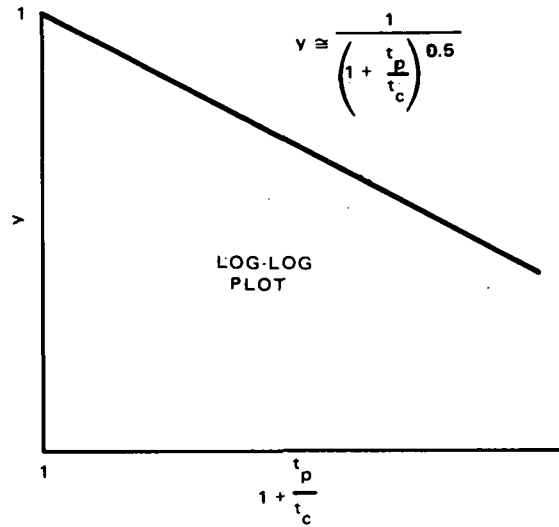


Figure 2-4. Shape of curve for semicircular edge.

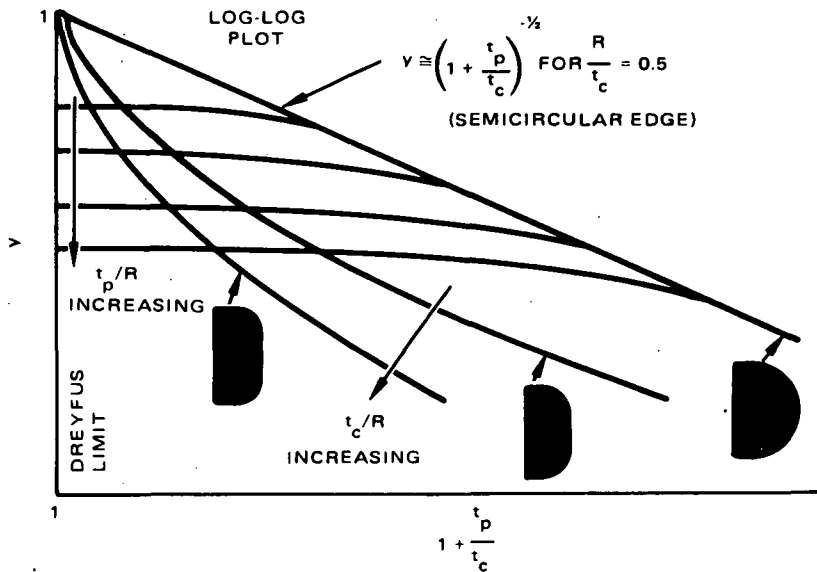


Figure 2-5. Shapes of master curves.

line with a slope of  $-0.5$  shown in Figure 2-4 as  $R/t_c \rightarrow 0.5$ . For fixed finite values of  $t_c/R$ , physical reasoning indicates that  $y \rightarrow 1$  as  $t_p/t_c \rightarrow 0$ , because the cell edge appears to be infinitely blunt in this limit (see Figure 1-3c).

The finite-element results were consistent with these deduced shapes. In fact, the numerical results indicated that, for each fixed finite value of  $t_c/R$ , the curve becomes parallel to the straight line for the semicircular edge for  $t_p/t_c > 2$ . That is,

$$y \propto \left(1 + \frac{t_p}{t_c}\right)^{-1/2} \text{ for } t_p/t_c > 2 \text{ and } t_c/R \text{ fixed.} \quad (2-9)$$

Pursuing this further, we cross-plotted  $y$  versus  $1 + (t_c/R)$  on log-log paper. For fixed values of  $t_p/t_c$ , the finite-element results turned out to be nearly (to within 10 percent) straight lines with a slope of  $-1/4$ , as shown in Figure 2-6. The parameter

$$1 + \frac{t_c}{R}$$

has a minimum value of 3, corresponding to the semicircular-edged cell ( $t_c/R = 2$ ). The parameter

$$1 + \frac{t_c}{R} - 2 = \frac{t_c}{R} - 1$$

has a minimum value of 1, as desired for a curve fit. Therefore, we deduced that

$$y \propto \left( \frac{t_c}{R} - 1 \right)^{-1/4} \text{ for } t_p/t_c > 2. \quad (2-10)$$

Thus we obtained the simple formula

$$y \cong \left( 1 + \frac{t_p}{t_c} \right)^{1/2} \left( \frac{t_c}{R} - 1 \right)^{-1/4} \text{ for } 2 \leq t_p/t_c \leq 100 \text{ and } R/t_c \geq 0.025. \quad (2-11)$$

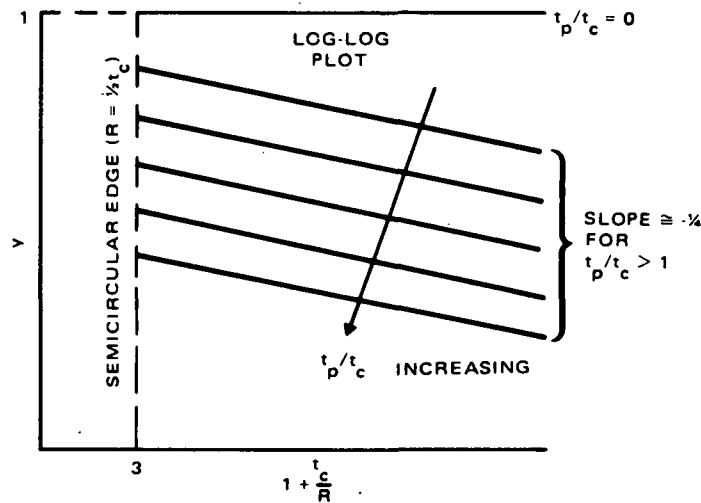


Figure 2-6. Shapes of curves for fixed  $t_p/t_c$ .

For  $t_p/t_c < 2$  and  $R/t_c < 0.5$ , the values of  $y$  predicted by the finite-element method agreed closely with those calculated by Dreyfus' solution for the thick-cell limit (Equations (2-2) and (2-3)). The Dreyfus solution appears to blend with the straight lines having slopes of  $-0.5$ .



The resultant master curves are plotted in Figure 2-7. The values predicted by the finite-element method also are shown on the graph. As was mentioned above, the values are given approximately by the Dreyfus solution (Equations (2-2) and (2-3)) for  $t_p/t_c < 2$  and the curve-fit formula (Equation (2-11)) for  $t_p/t_c > 2$ . For example, for  $t_p/t_c = 0.5$  and  $R/t_c = 0.025$ , we have

$$\frac{t_p}{R} = \frac{t_p}{t_c} \frac{t_c}{R} = \frac{0.5}{0.025} = 20.$$

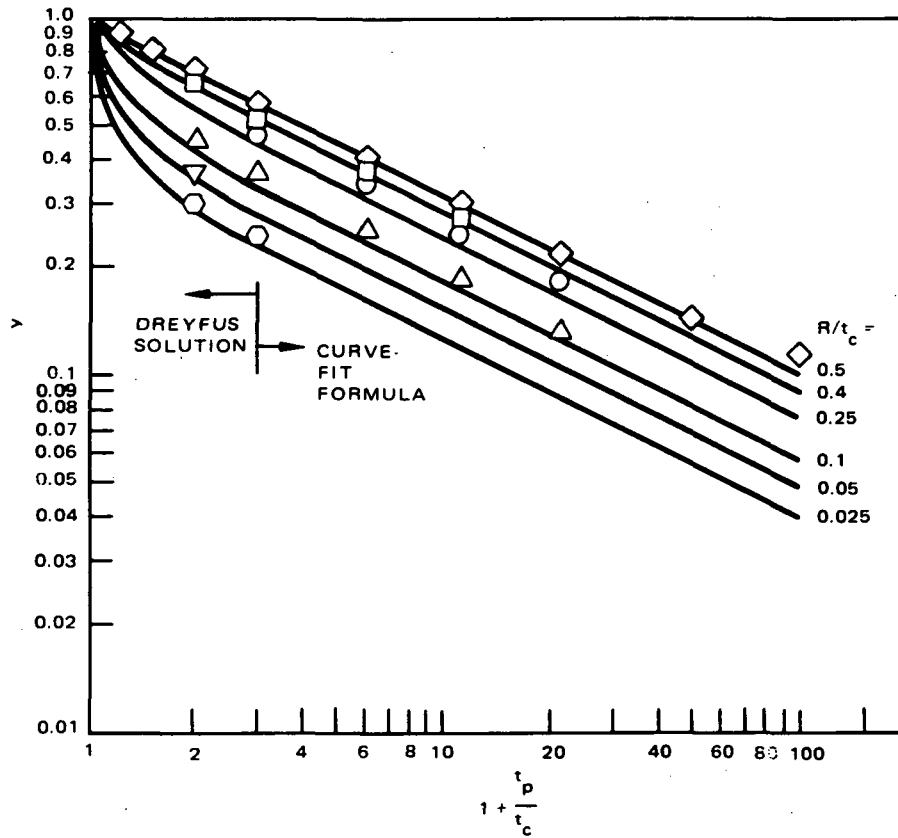


Figure 2-7. Master curves for electrical stress intensification.

The Dreyfus value is  $y = 0.37$ , and this value also is obtained from Figure 2-7. As another example, for  $t_p/t_c = 20$  and  $R/t_c = 0.1$ , Equation (2-11) yields

$$y \cong \frac{1}{\left(1 + \frac{t_p}{t_c}\right)^{1/2} \left(\frac{t_c}{R} - 1\right)^{1/4}} = \frac{1}{(1 + 20)^{1/2} (10 - 1)^{1/4}} = \frac{1}{(21)^{1/2} (9)^{1/4}} = 0.13,$$

as is obtained from Figure 2-7.

## 2.6 LOCATION OF MAXIMUM ELECTRIC FIELD

In addition to the value of the maximum electric field, the location of the maximum field is of interest to the designer. The locations determined by the finite-element method are shown in Figure 2-8 in terms of the angle  $\theta$  defined in the sketch in the figure.

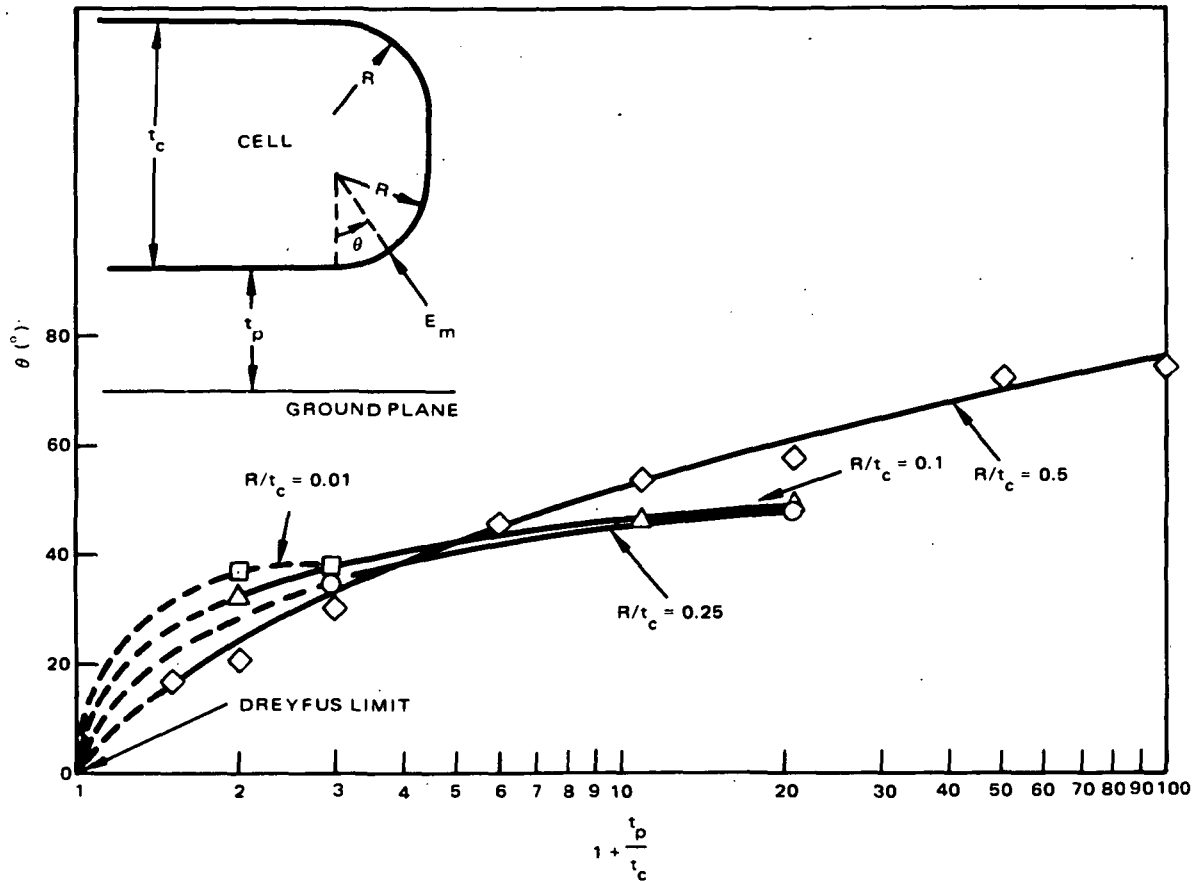


Figure 2-8. Location of maximum electric field.

For the thick-cell limit ( $t_p/t_c \rightarrow 0$ ), the Dreyfus solution yields  $\theta = 0$ . For each value of  $R/t_c$ , the finite-element values of  $\theta$  decrease with decreasing  $t_p/t_c$ . The dashed curves, obtained by extrapolating the finite-element values to  $t_p/t_c = 0$ , approach the Dreyfus limit, as they should; this is a check on the accuracy of the finite-element results.

To evaluate the limit of  $\theta$  as the cell becomes very thin, the values for the semicircular-edged cell were plotted versus  $t_c/t_p$  in Figure 2-9. The value of  $\theta$  appears to approach 90 degrees as the cell shape approaches an infinitesimally thin plane. This result is consistent with the exact solution obtained by Maxwell for this limiting shape (Ref. 4).

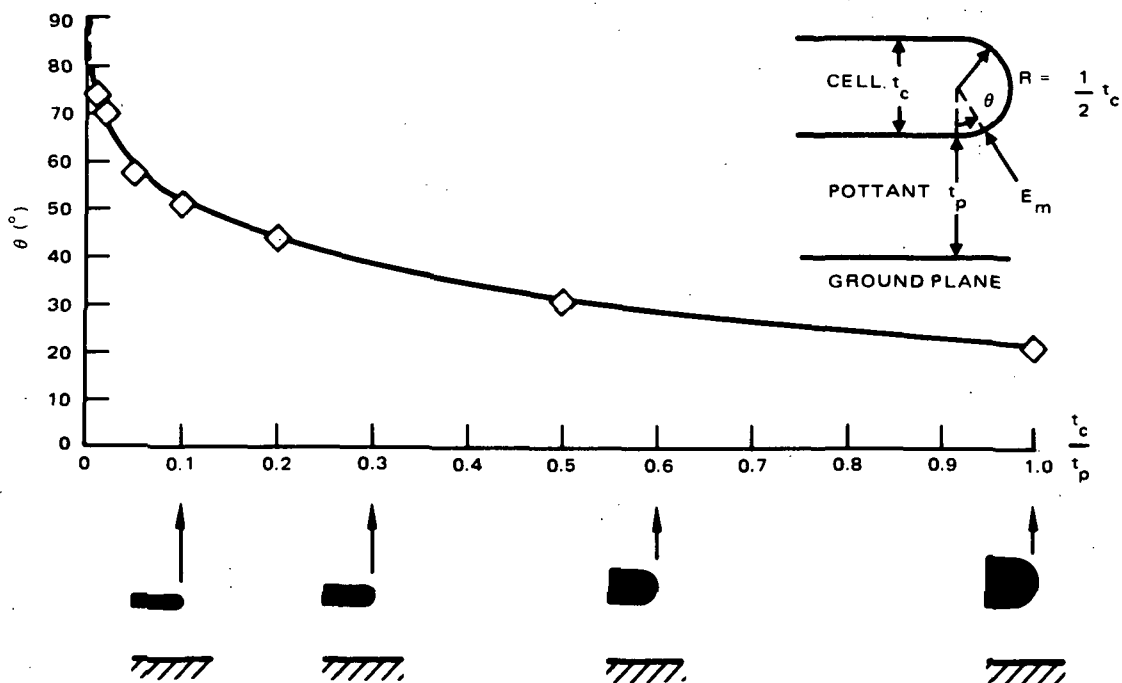


Figure 2-9. Location of maximum electric field on semicircular-edged cell — thin-cell limit.

## 2.7 APPLICATION OF RESULTS TO DESIGN OF PHOTOVOLTAIC MODULES

The results presented in Sections 2.5 and 2.6 provide quantitative information on the effects of the module design parameters on the magnitude and location of the maximum electric field.

- Effect of pottant thickness: For a given cell shape, the formulas in Section 2.5 enable the reduction in the maximum electric field obtained by increasing the pottant thickness to be evaluated. From Equations (2-1) and (2-11), the maximum electric field varies approximately, for large values of  $t_p/t_c$ , as

$$E_m \propto \left( \frac{t_p}{t_c} \right)^{-1/2} \quad (2-12)$$

- Effect of cell shape: For a given pottant thickness, these formulas enable the intensification of the electric field produced by making the cell edge very sharp or the cell very thin to be estimated. Figure 2-7 shows that very small values of  $y$  occur only with very sharp edges (as in Figure 1-3a) or very thin cells (Figure 1-3b).

## 2.8 AREA FOR FURTHER INVESTIGATION

Because the formula (2-11) was obtained by curve fitting the finite-element results, its accuracy for very thin cells is uncertain. Therefore an investigation of the asymptotic behavior of  $y$  in the thin-cell limit would be useful for designers of thin-film photovoltaic modules. The objective would be to evaluate mathematically whether the asymptotic dependence actually is the simple  $1/2$  power dependence in Equation (2-11) or another relationship.

A combination of several mathematical techniques appears capable of achieving this objective. These tools include conformal mapping (for example, Ref. 8) and perturbation methods (Ref. 9).

### 3.0 CALCULATION OF LINES OF FORCE OF THREE-DIMENSIONAL ELECTRIC FIELDS

This section documents the application of the spline method in the calculation of lines of force on planes of symmetry of three-dimensional electric fields.

#### 3.1 INTRODUCTION

We present the result of the calculation of the lines of force on planes of symmetry for the geometry used in the JPL electrochemical corrosion studies (Ref. 10). To our best knowledge, no existing method is available in NASTRAN or elsewhere to perform this task. Therefore we developed a method to calculate lines of force, given the NASTRAN output consisting of the values of the potential at discrete points. The algorithm we developed uses the method of cubic splines. However, extensions were made to account for non-rectangular domains and free spline boundary conditions. Section 3.2 gives a brief description of the basic equations. The numerical method is outlined in Section 3.3. Finally, the calculations for the electrochemical corrosion test geometry are discussed in Section 3.4.

#### 3.2 BASIC EQUATIONS

Some of the following material is a summary of Ref. 11. Let the three dimensional function  $\phi(x, y, z)$  be the electrostatic potential. At any arbitrary point  $P(x, y, z)$ , let  $\mathbf{ds}$  be an element of the line of force passing through  $P$ . (Boldface symbols denote vector quantities.) Then  $\mathbf{ds}$  must be parallel to the electric field intensity  $\mathbf{E}$  at  $P$ . That is,

$$\mathbf{ds} \times \mathbf{E} = 0, \quad (3-1)$$

where  $\mathbf{E}$  has Cartesian components  $(\phi_x, \phi_y, \phi_z)$ . (The subscripts  $x, y, z$  denote partial derivatives. For example,  $\phi_x$  denotes  $\partial\phi/\partial x$ .) This can also be written as

$$\frac{dx}{\phi_x} = \frac{dy}{\phi_y} = \frac{dz}{\phi_z} \quad (3-2)$$

Equations (3-2) for the unknowns  $x$ ,  $y$ , and  $z$  have two independent solutions:

$$\begin{aligned}\psi_1(x, y, z) &= c_1, \\ \psi_2(x, y, z) &= c_2,\end{aligned}\tag{3-3}$$

where  $c_1$  and  $c_2$  are constants. Therefore, at every point  $P$ , there exist two stream functions. To obtain the relationship between the electric field intensity and the stream functions  $\psi_1$  and  $\psi_2$ , we consider the following. The surfaces  $\psi_1 = c_1$  and  $\psi_2 = c_2$  intersect along the line of force  $L$ , (Figure 3-1). The electric field intensity  $E$  is normal to both  $\nabla\psi_1$  and  $\nabla\psi_2$  on  $L$ :

$$\begin{aligned}E \cdot \nabla\psi_1 &= 0, \\ E \cdot \nabla\psi_2 &= 0.\end{aligned}\tag{3-4}$$

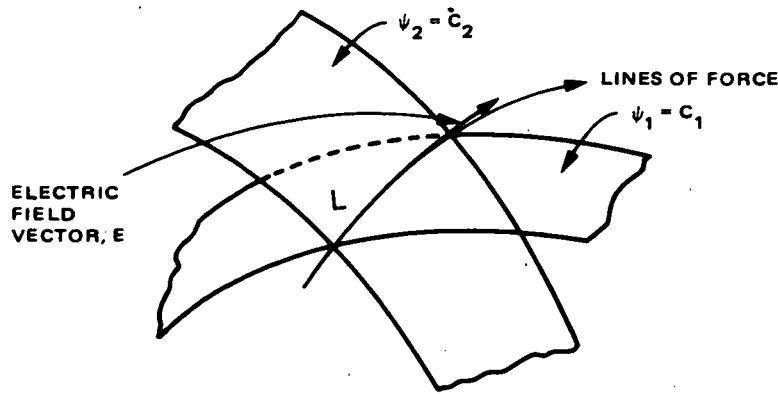


Figure 3-1. Lines of force and stream functions.

That is, the electric field intensity  $E$  is normal to the plane formed by the vectors  $\nabla\psi_1$  and  $\nabla\psi_2$ . Hence there exists a scalar function  $q(x, y, z) \neq \psi_1$  and  $\neq \psi_2$  such that

$$q(x, y, z) E = \nabla\psi_1 \times \nabla\psi_2.\tag{3-5}$$

For a region having uniform permittivity and no charges,

$$\nabla \cdot E = 0.\tag{3-6}$$

Taking the divergence of (3-5) and using the vector identity,

$$\nabla \cdot (\nabla\psi_1 \times \nabla\psi_2) = 0,\tag{3-7}$$

we have

$$E \cdot \nabla q = 0.\tag{3-8}$$

This implies that

$$q = \text{constant},$$

and we can set

$$q = 1. \quad (3-9)$$

Thus we obtain

$$\mathbf{E} = \nabla\psi_1 \times \nabla\psi_2.$$

For applications where solutions contain planes of symmetry, the equations for the lines of force greatly simplify. If we designate  $z = c$  as a plane of symmetry,  $\partial\phi/\partial z$  must be zero on  $z = c$ . Equations (3-2) for the lines of force on the plane of symmetry  $z = c$  have solutions

$$\begin{aligned} \psi_1(x, y; z = c) &= \psi(x, y), \\ \psi_2(x, y; z = c) &= \text{constant}. \end{aligned} \quad (3-10)$$

The intersections of the surfaces  $\psi_1 = c_1$  and  $\psi_2 = c_2$  are the lines of force. Hence, a set of lines of force lies on the plane of symmetry. On the plane of symmetry, the partial derivatives,  $\partial\psi_2/\partial x$ ,  $\partial\psi_2/\partial y$ , and  $\partial\psi_1/\partial z$  are zero. Substituting (3-10) into (3-5) on the plane of symmetry with  $q = 1$  yields the orthogonality conditions

$$\begin{aligned} \frac{\partial\psi}{\partial x} &= p(x, y) \frac{\partial\phi}{\partial y}, \\ \frac{\partial\psi}{\partial y} &= -p(x, y) \frac{\partial\phi}{\partial x}, \end{aligned} \quad (3-11)$$

where  $p(x, y) = (-\partial\psi_2/\partial z)^{-1}$ . Equation (3-11) is equivalent to the familiar orthogonality condition:

$$\frac{\partial\psi}{\partial x} \frac{\partial\phi}{\partial x} + \frac{\partial\psi}{\partial y} \frac{\partial\phi}{\partial y} \equiv \nabla\psi \cdot \nabla\phi = 0. \quad (3-12)$$

In general, on the plane of symmetry ( $z = c$ ), the second partial derivative with respect to  $z$  is nonzero:

$$\frac{\partial^2\psi}{\partial z^2} \neq 0. \quad (3-13)$$

Therefore the two-dimensional Laplacian is, in general, nonzero on the plane of symmetry  $z = c$ :

$$\frac{\partial^2\psi}{\partial x^2} + \frac{\partial^2\psi}{\partial y^2} \neq 0. \quad (3-14)$$

This implies that the multiplicative scalar function  $p(x, y)$  is not constant on the plane of symmetry.

For strictly two-dimensional problems,  $p = 1$ . To see this, the Cauchy-Riemann equations

$$\begin{aligned}\frac{\partial \psi}{\partial x} &= \frac{\partial \phi}{\partial y} \\ \frac{\partial \psi}{\partial y} &= -\frac{\partial \phi}{\partial x}\end{aligned}\tag{3-15}$$

imply that both the electrostatic potential and the stream function satisfy the two-dimensional Laplace equation:

$$\begin{aligned}\frac{\partial^2 \psi}{\partial x^2} + \frac{\partial^2 \psi}{\partial y^2} &= 0, \\ \frac{\partial^2 \phi}{\partial x^2} + \frac{\partial^2 \phi}{\partial y^2} &= 0.\end{aligned}$$

### 3.3 NUMERICAL METHOD FOR LINES OF FORCE ON PLANES OF SYMMETRY

If  $\phi$  is known everywhere on the plane of symmetry, equipotentials can easily be computed; and the lines of force can similarly be determined if  $\psi$  is known on the plane of symmetry. From now on, we shall assume we are treating the problem where the plane of symmetry is given by  $z = c$ .

However, we need to determine  $\psi$  if  $\phi$  is known only at discrete points. This can easily be done as follows. Given  $\phi$ , the method of splines is used to obtain the numerical approximations of the partial derivatives. Knowing the partial derivatives of  $\phi$ , the orthogonality condition (3-12) determines the partial derivatives of  $\psi$  up to the multiplicative function  $p(x, y; z = c)$ . Finally, the spline equations for the two partial derivatives  $\partial\psi/\partial x$  and  $\partial\psi/\partial y$  provide a system of linear equations for the numerical approximation of  $\psi$  and the multiplicative function  $p$ .

Section 3.3.1 gives a brief description of the method of splines for rectangular domains. An extension to incorporate free spline boundary conditions is given in Section 3.3.2, and the treatment of non-rectangular domains is discussed in Section 3.3.3. Next, the numerical algorithm for the calculation of the lines of force from the electrostatic potential is given in Section 3.3.4. Two illustrated examples are shown in Section 3.3.5 to verify the numerical method.

#### 3.3.1 Computation of Partial Derivatives of Function $\phi(x, y)$

Given the function values  $\phi_{ij} \equiv \phi(x_i, y_j)$ ,  $i = 1, 2, \dots, N$ ,  $j = 1, 2, \dots, M$ , on a rectangular mesh  $[x_i, y_j]$ , and partial derivatives on the boundary of the rectangle:  $\partial\phi/\partial y(x_i, y_1)$ ,



$\partial\phi/\partial y(x_i, y_M)$ ,  $i = 1, 2, \dots, N$ , and  $\partial\phi/\partial x(x_1, y_j)$ ,  $\partial\phi/\partial x(x_N, y_j)$ ,  $j = 1, 2, \dots, M$ , the method of cubic splines can be used to obtain the partial derivatives and  $\phi$  at every point inside the rectangle (see Ref. 12, Chapter 4). The method is efficient, accurate and stable.

### 3.3.2 Extensions to Free Spline Boundary Data

If the partial derivatives  $\partial\phi/\partial x$  and  $\partial\phi/\partial y$  are not prescribed on the boundary, additional conditions must be added to the spline equations. Here we give two alternatives:

Lagrange polynomial approximation—the partial derivatives on the boundary can be approximated by differentiating the Lagrange interpolation polynomial and evaluating at the boundary point. An advantage is that it preserves the order of the spline method; a disadvantage is its lack of efficiency.

Artificial boundary condition at a node adjacent to the boundary—to obtain a near tridiagonal matrix structure, the second derivative difference approximation is matched at the node adjacent to the boundary:

$$\frac{\frac{\partial\phi}{\partial x}(x_3) - \frac{\partial\phi}{\partial x}(x_1)}{2h} = \frac{\phi(x_3) - 2\phi(x_2) + \phi(x_1)}{h^2} \quad (3-16)$$

(For illustration, the above equation is written for the special case of uniform mesh,  $h$ ; the left hand side is the centered difference approximation to the first derivative of  $\partial\phi/\partial x$  at  $x = x_2$ , while the right hand side is the finite difference approximation of the second derivative of  $\phi$  at  $x = x_2$ .) An advantage is it is very efficient; a disadvantage of the artificial boundary condition is that it is only second order accurate.

Both alternatives require that the number of nodes,  $N$  and  $M$ , be greater than 3. This is not an altogether unreasonable constraint because many practical problems use more than 3 nodes for their numerical approximations.

### 3.3.3 Extension to Nonrectangular Domain With Quadrilateral Subelements

The spline method can be used for arbitrary nonrectangular domains by means of a change of variables. Specifically, let the physical plane coordinates  $(x, y)$  be functions of the transformed plane coordinates  $(r, s)$ . The standard method of splines with free spline boundary data extension (Section 3.3.2) can be used to compute the partial derivatives of  $x, y$  and  $\phi$  with respect to  $r$  and  $s$  in a rectangular domain in the  $rs$  plane. The partial derivatives of  $\phi$  with respect to  $x$  and  $y$  can be evaluated using the chain rule:

$$\frac{\partial\phi}{\partial x} \frac{\partial x}{\partial r} + \frac{\partial\phi}{\partial y} \frac{\partial y}{\partial r} = \frac{\partial\phi}{\partial r},$$

$$\frac{\partial \phi}{\partial x} \frac{\partial x}{\partial s} + \frac{\partial \phi}{\partial y} \frac{\partial y}{\partial s} = \frac{\partial \phi}{\partial s}.$$

Solving for  $\partial \phi / \partial x$  and  $\partial \phi / \partial y$ :

$$\begin{aligned} \frac{\partial \phi}{\partial x} &= \frac{\left( \frac{\partial \phi}{\partial r} \frac{\partial y}{\partial s} - \frac{\partial \phi}{\partial s} \frac{\partial y}{\partial r} \right)}{D}, \\ \frac{\partial \phi}{\partial y} &= \frac{\left( \frac{\partial \phi}{\partial s} \frac{\partial x}{\partial r} - \frac{\partial \phi}{\partial r} \frac{\partial x}{\partial s} \right)}{D}, \end{aligned} \quad (3-17)$$

where

$$D = \frac{\partial x}{\partial r} \frac{\partial y}{\partial s} - \frac{\partial x}{\partial s} \frac{\partial y}{\partial r}.$$

### 3.3.4 Computation of $\psi$ .

Knowing the partial derivatives of  $\phi$  at every point inside the nonrectangular domain, this section describes the final steps to obtain  $\psi$ .

The orthogonality conditions (3-11) are

$$\frac{\partial \psi}{\partial x} = p(x, y) \frac{\partial \phi}{\partial y},$$

$$\frac{\partial \psi}{\partial y} = -p(x, y) \frac{\partial \phi}{\partial x},$$

where the scalar multiplicative function  $p(x, y)$  is to be determined. (For the two-dimensional Laplace equation,  $p(x, y) = 1$ , and the more efficient method of line integration can be used to compute the stream function  $\psi$ .)

The partial derivatives of  $\psi$  with respect to  $r$  and  $s$  in the transformed plane are given by

$$\begin{aligned} \frac{\partial \psi}{\partial r} &= p(x, y) \left( \frac{\partial \phi}{\partial y} \frac{\partial x}{\partial r} - \frac{\partial \phi}{\partial x} \frac{\partial y}{\partial r} \right), \\ \frac{\partial \psi}{\partial s} &= p(x, y) \left( \frac{\partial \phi}{\partial y} \frac{\partial x}{\partial s} - \frac{\partial \phi}{\partial x} \frac{\partial y}{\partial s} \right). \end{aligned} \quad (3-18)$$

For uniqueness of the solution, we observe that, if  $\psi(x, y)$  is a function which satisfies the orthogonality condition (3-12), then  $\bar{\psi} = a + b \psi(x, y)$  also satisfies the orthogonality

condition, where  $a$  and  $b$  are arbitrary constants and  $b$  is nonzero:

$$\begin{aligned} \frac{\partial \phi}{\partial x} \frac{\partial \psi}{\partial x} + \frac{\partial \phi}{\partial y} \frac{\partial \psi}{\partial y} &= \frac{\partial \phi}{\partial x} \frac{\partial}{\partial x} (a + b \psi) + \frac{\partial \phi}{\partial y} \frac{\partial}{\partial y} (a + b \psi) \\ &= b \left( \frac{\partial \phi}{\partial x} \frac{\partial \psi}{\partial x} + \frac{\partial \phi}{\partial y} \frac{\partial \psi}{\partial y} \right) \\ &= 0. \end{aligned}$$

For uniqueness, we impose the following initial conditions:

$$\begin{aligned} \psi(\mathbf{r}_l, \mathbf{s}_l) &= 0, \\ p(\mathbf{r}_l, \mathbf{s}_l) &= \alpha, \end{aligned} \quad (3-19)$$

where  $\alpha$  is a nonzero constant.

The requirement that the second partial derivatives  $\partial^2\psi/\partial x^2$  and  $\partial^2\psi/\partial y^2$  of the cubic spline polynomial approximation of  $\psi$  be continuous at the interior nodes  $(x_i, y_j)$ ,  $i = 2, 3, \dots, (N-1)$ ,  $j = 2, 3, \dots, (M-1)$ , provides  $2(N-1)(M-1)$  linear equations. Furthermore, the application of the artificial boundary conditions (3-16) and the initial conditions (3-19) provide an additional  $2(N+M-1)$  linear equations. Adding, we have  $2MN$  linear equations for the  $2MN$  unknowns:  $\psi_{ij}$  and  $p_{ij}$ ,  $i = 1, 2, \dots, N$ , and  $j = 1, 2, \dots, M$ .

The system of linear equations can be put into the following form:

$$\mathcal{A}x \equiv \begin{bmatrix} A_{11} & A_{12} \\ & \\ & \\ A_{21} & A_{22} \end{bmatrix} \begin{bmatrix} p_1 \\ p_2 \\ \cdot \\ \cdot \\ \cdot \\ p_M \\ q_1 \\ q_2 \\ \cdot \\ \cdot \\ \cdot \\ q_M \end{bmatrix} = f. \quad (3-20)$$

Here  $A_{11}$  and  $A_{12}$  are block diagonal matrices with its elements being near-tridiagonal matrices of the form

$$\begin{bmatrix} x & x & x & & & & \\ x & x & x & & & & \\ & x & x & x & & & \\ & & x & x & x & & \\ & & & x & x & x & \\ & & & & x & x & x \\ & & & & & x & x & x \\ & & & & & & x & x & x \end{bmatrix} \quad (3-21)$$

$A_{21}$  and  $A_{22}$  are near-block-tridiagonal matrices having the same form as (3-21), with its elements being diagonal matrices; and

$$\begin{aligned} p_k &= (p_{k,1}, p_{k,2}, \dots, p_{k,N})^T \\ q_k &= (\psi_{k,1}, \psi_{k,2}, \dots, \psi_{k,N})^T \end{aligned} \quad (3-22)$$

for  $k = 1, 2, \dots, M$ . The right-hand side  $f$  is a  $(2NM)$ -vector given by

$$f_i = \begin{cases} \alpha & i = 1, \\ 0 & \text{otherwise.} \end{cases} \quad (3-23)$$

where  $\alpha$  is a constant.

The solution algorithm of the system of linear equations is straightforward. The matrix is factorized into block LU-form:

$$\mathcal{A} = \begin{pmatrix} I & 0 \\ L_{21} & I \end{pmatrix} \begin{pmatrix} A_{11} & A_{12} \\ 0 & U_{22} \end{pmatrix} \quad (3-24)$$

where

$$\begin{aligned} L_{21} &= A_{21} A_{11}^{-1}, \\ U_{22} &= A_{22} - L_{21} A_{12}. \end{aligned} \quad (3-25)$$

Since the submatrix  $A_{11}$  is a block diagonal matrix, its submatrices can each be factorized into LU-form by using a very efficient near-tridiagonal matrix algorithm. The submatrix  $L_{21}$  can then be very efficiently solved. The near-block-tridiagonal matrix  $U_{22}$  is further factorized into LU-form using a band matrix solver with partial column pivoting. Finally, the solution can be obtained in the usual way:

$$\begin{aligned} \begin{pmatrix} I & 0 \\ L_{21} & I \end{pmatrix} y &= f, \\ \begin{pmatrix} A_{11} & A_{12} \\ 0 & U_{22} \end{pmatrix} x &= y. \end{aligned} \quad (3-26)$$

### 3.3.5 Numerical Examples to Verify Method

In this section, we give two examples. The numerical program developed requires the following inputs:

- on the plane of symmetry,  $z = c$ , the physical coordinates  $(x_i, y_j)$ ,  $i = 1, 2, \dots, N$ ,  $j = 1, 2, \dots, M$  ( $N, M$  greater than 3);
- the potential  $\phi(x_i, y_j)$ .

The output from the program is the numerical approximation of  $\psi$  at the input physical coordinates.

In each example, the plane of symmetry is  $z = 0$ . On this plane,  $\partial\phi/\partial z = 0$ , but  $\partial^2\phi/\partial z^2 \neq 0$ , so that

$$\frac{\partial^2\phi}{\partial x^2} + \frac{\partial^2\phi}{\partial y^2} \neq 0.$$

#### Example 1: Circular equipotentials

$$\phi(x,y,z) = x^2 + y^2 - 2z^2.$$

The equipotentials in the plane of symmetry ( $z=0$ ) are circles centered at the origin. The lines of force are straight lines passing through the origin; this point is therefore a singularity of the stream function. The numerical approximation of  $\psi$  and the potential in the region  $1 \leq x \leq 2$ ,  $2 \leq y \leq 3$ , are given in Figure 3-2.

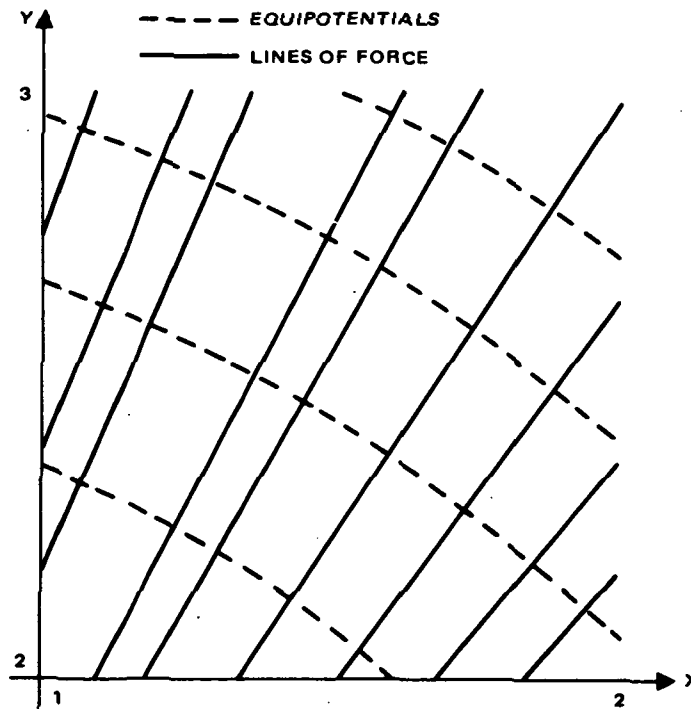


Figure 3-2. Equipotentials and lines of force for circular potentials of example 1.

### Example 2: Potential on a curved domain

$$\phi(x,y,z) = \exp(-x-0.5y) \cos(\sqrt{1.25} z)$$

for  $x$  and  $y$  lying in the region given by

$$x(r,s) = r(r+2)/3 + s(s+1)/2$$

$$y(r,s) = 2 - [r(r+3)/4 - s(s+2)/3]$$

for both  $r$  and  $s$  between 0 and 1.

This example demonstrated the validity of the theory and the numerical technique given above. In Table 3-1, we have the given  $\phi$ , the computed  $\psi$  and the computed  $p$ . In Table 3-2, we have the partial derivatives  $\phi_x$  and  $\phi_y$ , computed using the numerical method discussed above; also the partial derivatives  $\psi_x$  and  $\psi_y$  shown in the same table are computed using the same numerical procedure with the input obtained from the output of the numerical algorithm discussed in Section 3.3.4. The rightmost column in Table 3-2 gives the residual  $\phi_x\psi_x + \phi_y\psi_y$ , where the partial derivatives are the values obtained from cubic splines. To within the accuracy of our numerical method, the computed  $\psi$  is orthogonal to the given  $\phi$ . The exact equipotential and the computed lines of force are shown in Figure 3-3.

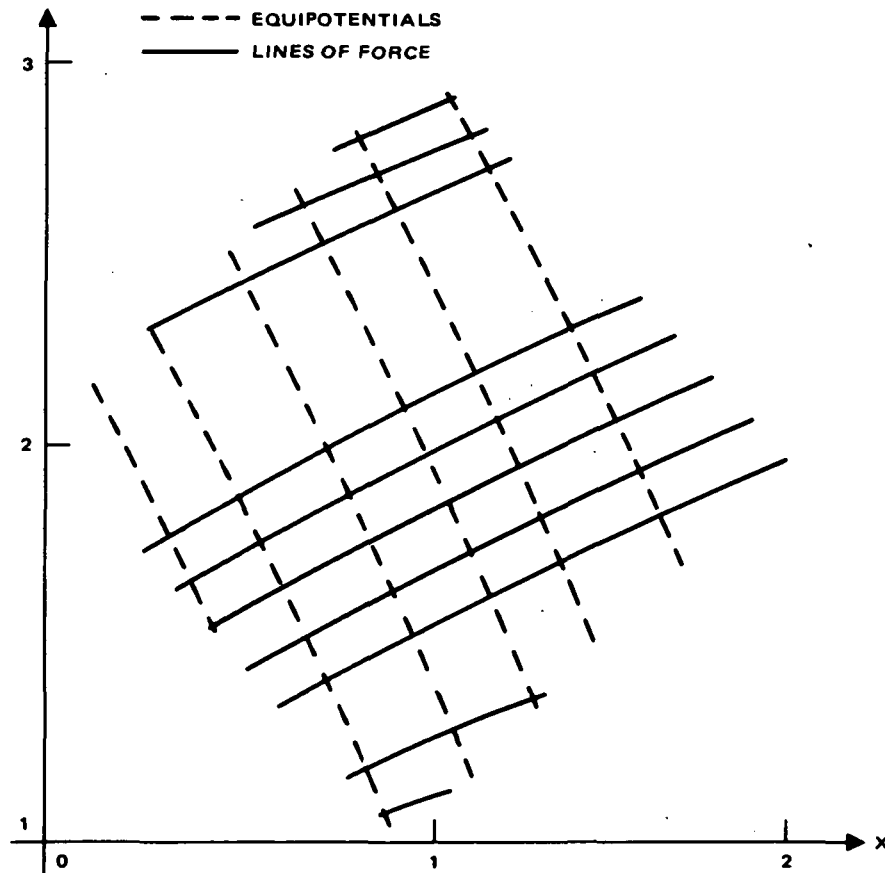


Figure 3-3. Equipotentials and lines of force for example 2.

TABLE 3-1. THE EXACT  $\phi; \psi$  AND  $p(x,y)$  COMPUTED FROM ALGORITHM

x	y	$\phi$	$\psi$	p
0.00000E+00	0.20000E+01	0.36788E+00	-0.12305E-14	0.50000E-02
0.14667E+00	0.18400E+01	0.34415E+00	0.38720E-02	0.40947E+00
0.32000E+00	0.16600E+01	0.31564E+00	0.74625E-01	0.10950E+01
0.52000E+00	0.14600E+01	0.28650E+00	0.17829E+00	0.10259E+01
0.74667E+00	0.12400E+01	0.25496E+00	0.23417E+00	0.70334E-01
0.10000E+01	0.10000E+01	0.22313E+00	0.16683E+00	-0.17821E+01
0.12000E+00	0.21467E+01	0.30321E+00	0.11288E-01	-0.75136E+00
0.26667E+00	0.19867E+01	0.28365E+00	-0.52079E-02	0.22379E+00
0.44000E+00	0.18067E+01	0.26097E+00	0.46182E-01	0.11708E+01
0.64000E+00	0.16067E+01	0.23614E+00	0.15078E+00	0.14225E+01
0.86667E+00	0.13867E+01	0.21014E+00	0.22881E+00	0.49600E+00
0.11200E+01	0.11467E+01	0.18391E+00	0.19692E+00	-0.16133E+01
0.28000E+00	0.23200E+01	0.23693E+00	0.38292E-01	-0.14458E+01
0.42667E+00	0.21600E+01	0.22165E+00	-0.61800E-02	-0.20786E+00
0.60000E+00	0.19800E+01	0.20393E+00	0.20573E-01	0.11800E+01
0.80000E+00	0.17800E+01	0.18452E+00	0.11839E+00	0.19230E+01
0.10267E+01	0.15600E+01	0.16420E+00	0.21511E+00	0.11447E+01
0.12800E+01	0.13200E+01	0.14370E+00	0.21952E+00	-0.13106E+01
0.48000E+00	0.25200E+01	0.17552E+00	0.77270E-01	-0.24880E+01
0.62667E+00	0.23600E+01	0.16420E+00	0.49248E-02	-0.10780E+01
0.80000E+00	0.21800E+01	0.15107E+00	0.88810E-03	0.98297E+00
0.10000E+01	0.19800E+01	0.13670E+00	0.82985E-01	0.25472E+01
0.12267E+01	0.17600E+01	0.12164E+00	0.19242E+00	0.21560E+01
0.14800E+01	0.15200E+01	0.10646E+00	0.23261E+00	-0.69358E+00
0.72000E+00	0.27467E+01	0.12328E+00	0.12734E+00	-0.39624E+01
0.86667E+00	0.25867E+01	0.11533E+00	0.31001E-01	-0.26733E+01
0.10400E+01	0.24067E+01	0.10610E+00	-0.85961E-02	0.24581E+00
0.12400E+01	0.22067E+01	0.96007E-01	0.47698E-01	0.32068E+01
0.14667E+01	0.19867E+01	0.85435E-01	0.16128E+00	0.37150E+01
0.17200E+01	0.17467E+01	0.74770E-01	0.23419E+00	0.57047E+00
0.10000E+01	0.30000E+01	0.82085E-01	0.18196E+00	-0.56632E+01
0.11467E+01	0.28400E+01	0.76791E-01	0.72874E-01	-0.55612E+01
0.13200E+01	0.26600E+01	0.70651E-01	-0.33360E-02	-0.17128E+01
0.15200E+01	0.24600E+01	0.63928E-01	0.16772E-01	0.36455E+01
0.17467E+01	0.22400E+01	0.56888E-01	0.12317E+00	0.61634E+01
0.20000E+01	0.20000E+01	0.49787E-01	0.22279E+00	0.31500E+01

TABLE 3-2. PARTIAL DERIVATIVES COMPUTED USING CUBIC SPLINES,  
AND THE RESIDUALS  $\equiv \phi_x \psi_x + \phi_y \psi_y$

x	y	$\frac{\partial \phi}{\partial x}$	$\frac{\partial \phi}{\partial y}$	$\frac{\partial \psi}{\partial x}$	$\frac{\partial \psi}{\partial y}$	Residual
0.0000E+00	0.2000E+01	-0.36894E+00	-0.18501E+00	0.92504E-03	0.18447E-02	-0.18531E-14
0.14667E+00	0.18400E+01	-0.34520E+00	-0.17304E+00	0.70853E-01	-0.14135E+00	0.26246E-13
0.32000E+00	0.16800E+01	-0.31756E+00	-0.15923E+00	0.17433E+00	-0.34773E+00	0.19574E-12
0.52000E+00	0.14600E+01	-0.28732E+00	-0.14409E+00	0.14782E+00	-0.29476E+00	0.16708E-12
0.74667E+00	0.12400E+01	-0.25569E+00	-0.12822E+00	0.90182E-02	-0.17984E-01	0.17402E-13
0.10000E+01	0.10000E+01	-0.22370E+00	-0.11227E+00	0.20007E+00	0.39867E+00	-0.31139E-12
0.12000E+00	0.21467E+01	-0.30287E+00	-0.15141E+00	0.11376E+00	0.22757E+00	-0.60674E-13
0.26667E+00	0.19867E+01	-0.28341E+00	-0.14158E+00	0.35250E-01	-0.66546E-01	-0.56886E-03
0.44000E+00	0.18067E+01	-0.26074E+00	-0.13027E+00	0.15167E+00	-0.30453E+00	0.12326E-03
0.64000E+00	0.16067E+01	-0.23593E+00	-0.11787E+00	0.16787E+00	-0.33579E+00	-0.28323E-04
0.86667E+00	0.13867E+01	-0.20997E+00	-0.10487E+00	0.51922E-01	-0.10406E+00	0.11343E-04
0.11200E+01	0.11467E+01	-0.18371E+00	-0.91822E-01	0.14797E+00	0.29624E+00	-0.18035E-04
0.28000E+00	0.23200E+01	-0.23695E+00	-0.11856E+00	0.17142E+00	0.34258E+00	0.16248E-12
0.42667E+00	0.21600E+01	-0.22172E+00	-0.11087E+00	-0.23899E-01	0.46908E-01	0.97918E-04
0.60000E+00	0.19800E+01	-0.20398E+00	-0.10202E+00	0.12059E+00	-0.24090E+00	-0.21237E-04
0.80000E+00	0.17800E+01	-0.18457E+00	-0.92311E-01	0.17746E+00	-0.35486E+00	0.48835E-05
0.10267E+01	0.15600E+01	-0.16425E+00	-0.82137E-01	0.94043E-01	-0.18803E+00	-0.19570E-05
0.12800E+01	0.13200E+01	-0.14371E+00	-0.71918E-01	-0.94300E-01	0.18840E+00	0.31126E-05
0.48000E+00	0.25200E+01	-0.17541E+00	-0.87725E-01	-0.21826E+00	0.43642E+00	-0.18211E-12
0.62667E+00	0.23600E+01	-0.16414E+00	-0.82029E-01	-0.88205E-01	0.17671E+00	-0.17504E-04
0.80000E+00	0.21800E+01	-0.15101E+00	-0.75477E-01	0.74139E-01	-0.14838E+00	0.37992E-05
0.10000E+01	0.19800E+01	-0.13664E+00	-0.68293E-01	0.17397E+00	-0.34806E+00	-0.87415E-06
0.12267E+01	0.17600E+01	-0.12160E+00	-0.60765E-01	0.13100E+00	-0.26216E+00	0.35049E-06
0.14800E+01	0.15200E+01	-0.10640E+00	-0.53205E-01	-0.36891E-01	0.73784E-01	-0.55763E-06
0.72000E+00	0.27467E+01	-0.12348E+00	-0.61860E-01	-0.24512E+00	0.48927E+00	-0.10300E-12
0.86667E+00	0.25867E+01	-0.11553E+00	-0.57850E-01	-0.15476E+00	0.30897E+00	0.53382E-05
0.10400E+01	0.24067E+01	-0.10629E+00	-0.53234E-01	0.13109E-01	-0.26152E-01	-0.11590E-05
0.12400E+01	0.22067E+01	-0.96170E-01	-0.48172E-01	0.15447E+00	-0.30839E+00	0.26674E-06
0.14667E+01	0.19867E+01	-0.85583E-01	-0.42864E-01	0.15924E+00	-0.31794E+00	-0.10698E-06
0.17200E+01	0.17467E+01	-0.74881E-01	-0.37533E-01	0.21406E-01	-0.42712E-01	0.17021E-06
0.10000E+01	0.30000E+01	-0.81376E-01	-0.40440E-01	0.22902E+00	0.46085E+00	0.93873E-13
0.11467E+01	0.28400E+01	-0.76160E-01	-0.37796E-01	-0.21001E+00	0.42333E+00	-0.61889E-05
0.13200E+01	0.26600E+01	-0.70079E-01	-0.34765E-01	-0.59588E-01	0.12008E+00	0.13456E-05
0.15200E+01	0.24600E+01	-0.63418E-01	-0.31448E-01	0.11465E+00	-0.23120E+00	-0.31002E-06
0.17467E+01	0.22400E+01	-0.56443E-01	-0.27975E-01	0.17241E+00	-0.34788E+00	0.12445E-06
0.20000E+01	0.20000E+01	-0.49391E-01	-0.24491E-01	0.77153E-01	-0.15559E+00	-0.19813E-06



### 3.4 LINES OF FORCE FOR THE ELECTROCHEMICAL CORROSION TEST GEOMETRY

For the details of the electrochemical corrosion test see Ref. 10. We present here the numerical solution  $\psi$  on the two planes of symmetry indicated in Figure 3-4. The electrodes were cylinders having quarter-circular cross sections. The electrode thickness was small compared with the electrode radius, and the spacing between the electrodes also was small compared with the electrode radius. The planes of symmetry ABCDEFG and AHIJKB are perpendicular to each other. The plane ABCDEFG (the  $z = 0.023$  plane) is perpendicular to the axes of the cylindrical electrodes and is the midplane of the electrodes. The plane AHIJKB (the  $y = 0$  plane) contains the axes of the cylindrical electrodes. The intersection of these planes is the line connecting the centers of the electrodes (this line is parallel to the x-axis). Point A is the midpoint of this line ( $V = 1/2$ ), and B is the intersection of this line with the high-voltage electrode ( $V = 1$ ). Point D is in the  $x = 0$  plane at the corner of the high-voltage electrode. Point E is in the  $x = 0$  plane at the edge of the dielectric used in the electrochemical corrosion tests. Point C is on the high-voltage electrode. Point F is on a line parallel to the x-axis passing through E, and G is on a line parallel to the x-axis passing through C. Point K is at the edge of the high-voltage electrode, and H is on the  $V = 1/2$  plane on a line parallel to the x-axis passing through K. Point I is on the  $V = 1/2$  plane at the edge of the dielectric, and J is at the edge of the dielectric on a line passing through B and K.

Figures 3-5 through 3-7 give the solution for the region ABCDEFG. Figures 3-8 and 3-9 give the solution for the region AHIJKB. The number shown at a given point in Figures 3-6, 3-7 and 3-9 is the value of the stream function. The lines of force are the curves connecting the points having equal values of the stream function. Note that the y-scale is different from the x-scale in Figures 3-6 and 3-7; because of the different scales, perpendicular lines do not appear to be perpendicular; thus the lines of force do not appear to be perpendicular to the electrode.

The lines of force—electrostatic potential solution is said to be singular at a point  $Q(x,y,z=c)$  on the plane of symmetry if  $\phi_x = \phi_y = 0$ . At the point Q, the stream function is multi-valued. The numerical algorithm presented in Section 3.3 cannot handle this type of singularity. Such singularities occur in our geometry at the points D and K in Figure 3-4. We do not include the singularities in our computations.

Because of the acute scaling of the modelled cell, the NASTRAN model has only five points on lines parallel to AB in Figure 3-8. Consequently the NASTRAN numerical approximation along AB is coarse. Our calculation of the partial derivatives along AB does not possess the symmetric behaviour of the exact solution. To compensate for this deficiency, the numerical algorithm in Section 3.3.3 is modified: the symmetry boundary condition

$$\frac{\partial \phi}{\partial x} = 0$$

is applied along AB instead of the artificial boundary condition (3-16).

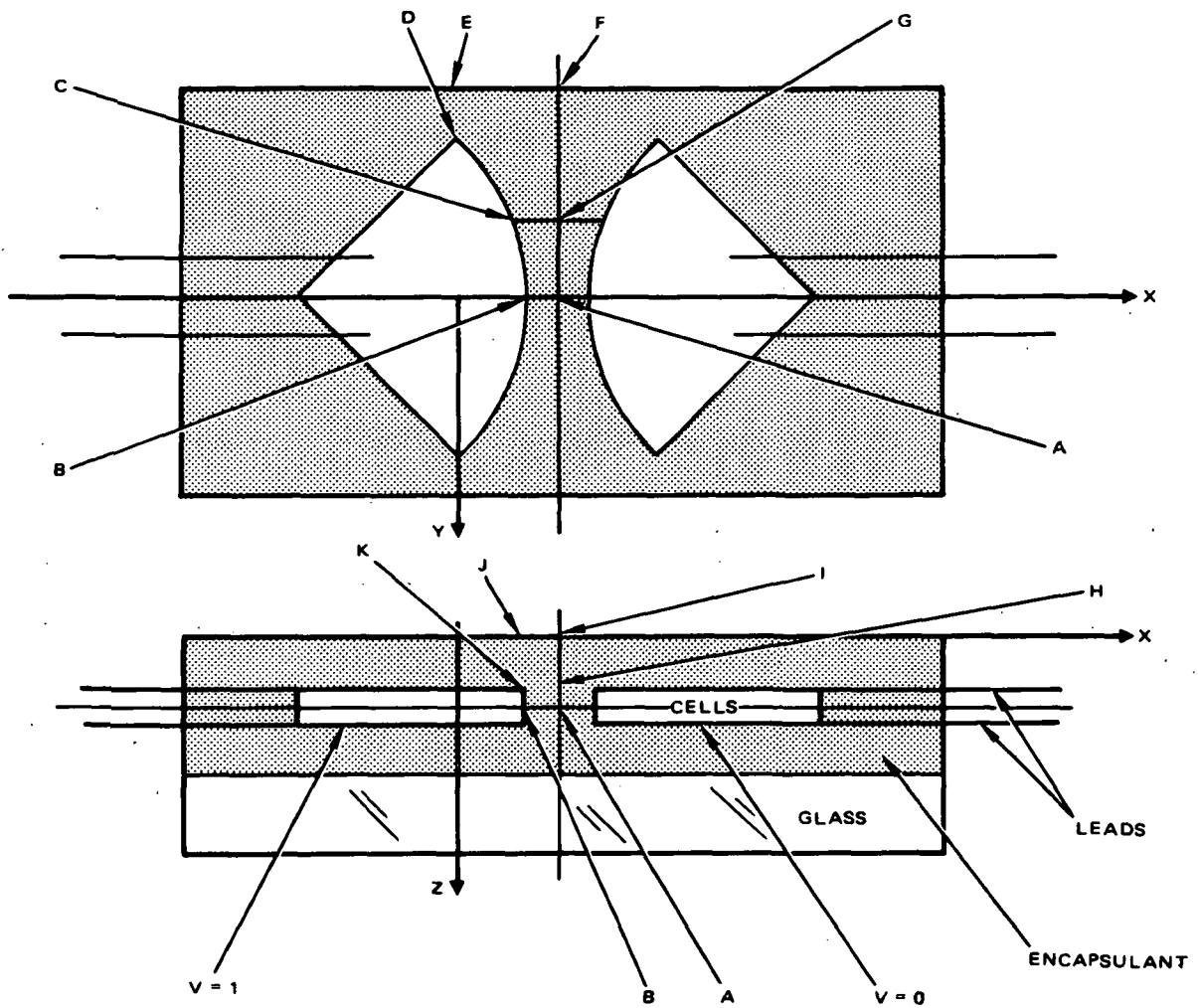


Figure 3-4. Electrochemical corrosion test specimen geometry.

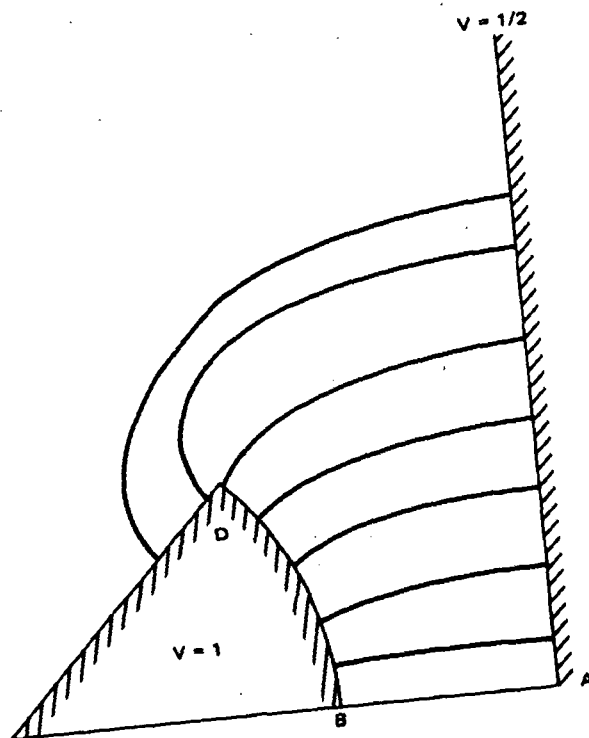


Figure 3-5. ABCDEFG plane — qualitative.

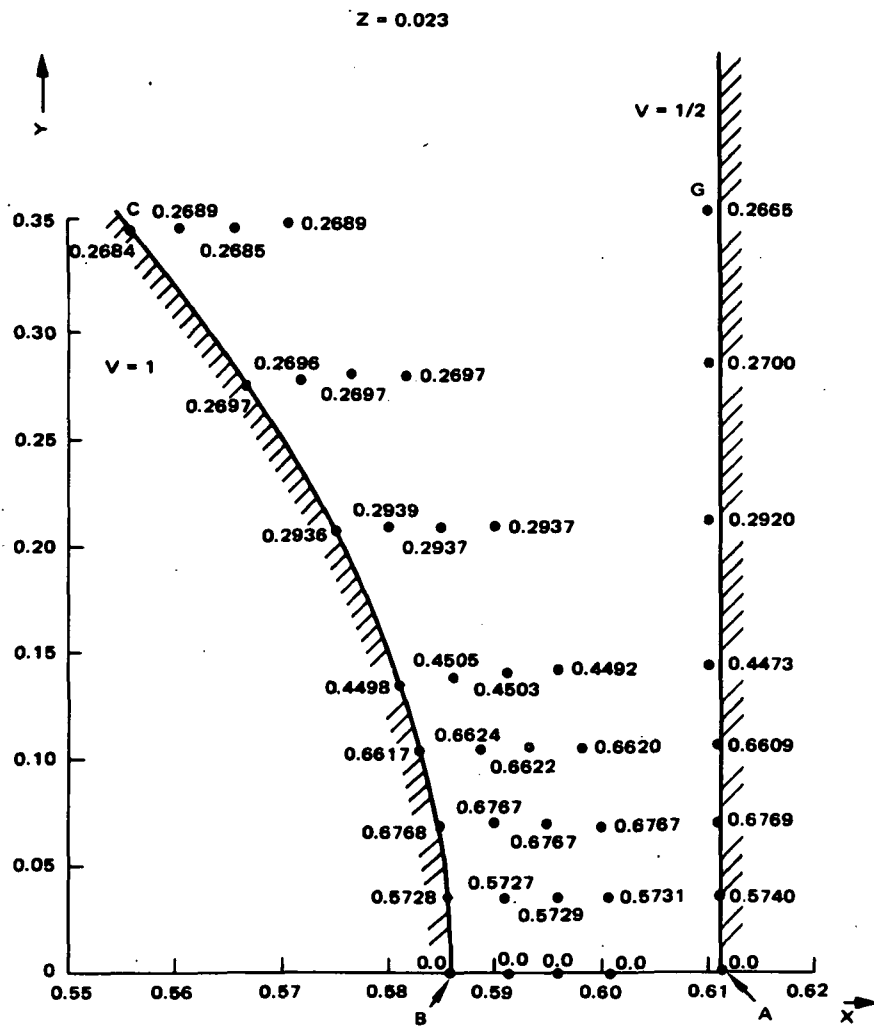


Figure 3-6. ABCDEFG plane – quantitative (near AB).



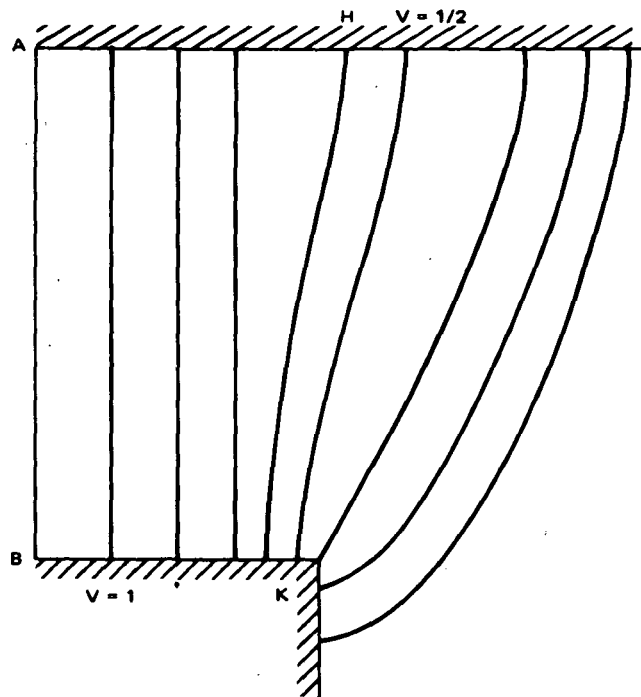
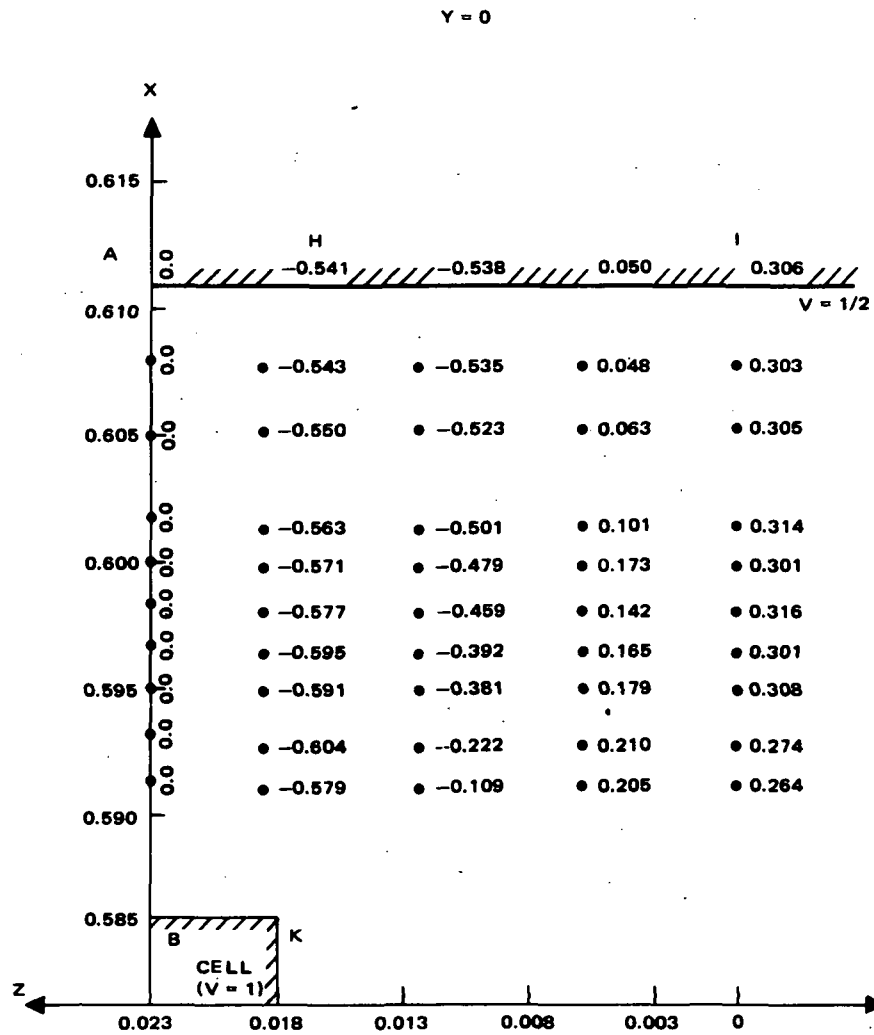


Figure 3-8. AH IJKB plane – qualitative.



#### 4.0 CONCLUSIONS

1. Quantitative information on the effect of photovoltaic module design parameters on the magnitude and location of the maximum electric field has been developed.
2. For a family of solar-cell-like shapes, simple formulas for calculating the electrical stress intensification at the cell edge have been developed.
3. The electrical stress intensification is severe only for cells having very sharp edges or for very thin cells.
4. The finite-element method is accurate for modules not having any of the extreme geometries mentioned in the preceding conclusion.
5. For extreme geometries—1) cells having sharp edges, 2) thin cells, or 3) blunt-edged cells or thin pottants—the finite-element results can be extrapolated by means of the simple formulas.
6. A method for calculating the lines of force for three-dimensional electric fields has been developed.



## 5.0 RECOMMENDATION

A mathematical investigation of the asymptotic behavior of electrical stress intensification for thin cells should be performed to verify what should be the design guidelines for advanced thin-film photovoltaic modules.

## ACKNOWLEDGEMENTS

Technical discussions with E.F. Cuddihy, R.G. Ross, G.R. Mon, A. Garcia, E.R. Bunker, and I.R. Jones were very helpful for the work described herein.

## REFERENCES

1. A. Garcia, C.P. Minning, and E.F. Cuddihy, "An Analytical Approach to Photovoltaic Encapsulation System Design," *Proc. 15th IEEE Photovoltaic Specialists Conf.*, pp. 460-465, May 1981.
2. A. Garcia, C.P. Minning, and E.F. Cuddihy, "Empirical Testing of an Analytical Model Predicting Electrical Isolation of Photovoltaic Modules," *Proc. 16th IEEE Photovoltaic Specialists Conf.*, pp. 1014-1019, September 1982.
3. J.M. Kallis, D.C. Trucker, E.F. Cuddihy, and A. Garcia, "Method for Calculating Multidimensional Electric Fields in Photovoltaic Modules," to be published in *Solar Cells*, Vol. 11, No. 4, pp. 309-330, 1984.
4. A. Schwaiger, *Theory of Dielectrics*, translated by R.W. Sorenson, pp. 106-110, John Wiley and Sons, New York, 1932.
5. A. Bouwers and P.G. Cath, "The Maximum Electrical Field Strength for Several Simple Electrode Configurations," *Philips Technical Review*, Vol.6, pp. 270-278, September 1941.
6. L. Dreyfus, "On the Application of the Theory of Conformal Representation to the Calculation of the Puncture and Flashover Voltages between Edges of Construction Elements under Oil" (in German), *Archiv fur Elektrotechnik*, Vol. XIII, pp. 123-145, 1924.

7. E.F. Cuddihy, "Some Technical Thoughts about Electrical Insulation Behavior," Jet Propulsion Laboratory Interoffice Memorandum 354-030-EFC:cy, 6 April 1983.
8. J.D. Cockroft, "The Effect of Curved Boundaries on the Distribution of Electrical Stress Round Conductors," *J. Institution of Electrical Engineers*, Vol. 66, pp. 385-409, 1928.
9. M. Van Dyke, *Perturbation Methods in Fluid Mechanics*, Academic Press, New York, 1964.
10. G.R. Mon, J. Orehotsky, R.G. Ross Jr., and G. Whitla, "Predicting Electrochemical Breakdown in Terrestrial Photovoltaic Modules," 17th IEEE Photovoltaic Specialists Conf., May 1984.
11. K. Karamcheti, *Principles of Ideal-Fluid Aerodynamics*, pp. 165-170, 276-277, John Wiley & Sons, 1969.
12. M. Schultz, *Spline Analysis*, Prentice Hall, 1973.

HAC Report No. FR-84-72-600

HAC Ref. No. E4677

APPENDIX B

**STRUCTURAL ANALYSIS  
PHASE 3C**

**L. B. Duncan  
Hughes Aircraft Company  
El Segundo, California**

**March 1984**

**Submitted to Spectrolab, Inc., to document  
part of the work performed on "Design, Analysis,  
and Test Verification of Advanced  
Encapsulation Systems"  
Spectrolab Contract No. 88774  
a subcontract of  
Jet Propulsion Laboratory Contract No. 955567**

## CONTENTS

	Page
INTRODUCTION .....	56
DISCUSSION .....	56
SOLAR CELL STRESS WITHOUT MODULE BENDING .....	57
RESULTS .....	60
ADDITIONAL CONSIDERATIONS .....	63
1. Solar Cell Length .....	63
2. Biaxial Material Properties .....	64
ACKNOWLEDGEMENTS .....	65
REFERENCES .....	65

## ILLUSTRATIONS

Figure		Page
1	Finite-element structural model for determination of stresses in module construction elements in vicinity of a centrally located cell .....	57
2	Deflection of structural panel, pottant and cell for 100°C temperature excursion .....	57
3	Model of three laminated layers .....	58
4	Cell stress for a glass structural panel, EVA pottant, $\Delta T = 100^{\circ}\text{C}$ , 4 in. x 4 in. x 0.001 in. silicon cell .....	60
5	Cell stress for a wood structural panel, EVA pottant, $\Delta T = 100^{\circ}\text{C}$ , 4 in. x 4 in. x 0.001 in. silicon cell .....	61
6	Cell stress for a steel structural panel, EVA pottant, $\Delta T = 100^{\circ}\text{C}$ , 4 in. x 4 in. x 0.001 in. silicon cell .....	61
7	Pottant shear stress .....	63
8	Master curve for thermal stress analysis .....	64
9	Master curve for pressure stress analysis .....	65

## SUMMARY

In the first phase of the encapsulation contract, finite element analyses were performed to predict solar cell stress due to uniform temperature changes of the flat-plate terrestrial photovoltaic modules. The results of the analyses were translated into a generalized master curve which provided a desktop capability for predicting cell stress for any combination of cell, pottant, and structural panel.

The finite element analyses assumed that out-of-plane bending of the module occurs. The degree of out-of-plane bending is unknown. To evaluate the bending assumption, the cell stresses were calculated in the present phase of the contract with the assumption that no out-of-plane bending occurs.

For small pottant thicknesses, the cell stress is 10-25 percent higher without bending than with bending; this difference is within the overall accuracy of the analysis. For large pottant thicknesses, the cell stress is 25 percent lower without bending than with bending, for glass and wood structural panels having thicknesses of 0.125 in. and 0.25 in., respectively. For a 0.08 in. thick steel panel, cell stress is always higher without bending than with bending.

The master curves derived previously for predicting the cell stress can be used as presented originally, with the following exceptions:

- The master curve for solar cell thermal stress analysis should not be used for a cell length greater than 4 inches.
- For beam-like solar cells, the elastic modulus,  $E$ , should be input to the master curves to compute solar cell stresses. For round or plate-like solar cells, the quantity  $E / (1 - \nu)$  should be used, where  $\nu$  = Poisson's ratio.

## INTRODUCTION

In the first phase of the encapsulation contract, finite element analyses were performed to predict solar cell stress due to uniform temperature changes of the flat-plate, terrestrial, photovoltaic modules (Reference 1). The boundary conditions imposed on the finite element model permitted out-of-plane bending as well as change in length of the cell, pottant, and structural panel laminate. The results of the analyses were translated into a generalized master curve which provided a desktop capability for predicting cell stress for any combination of cell, pottant, and structural panel (Reference 2).

In the current phase of the contract, closed-form analyses were performed to predict temperature-induced solar cell stress when out-of-plane bending is not permitted. This report presents a comparison of the results of the no-bending closed-form analyses to the results of the with-bending finite element analyses in order to evaluate the sensitivity of solar cell stress to the out-of-plane bending boundary condition.

In addition, the accuracy of the solar cell stress master curves for temperature and pressure loading of the module are discussed.

## DISCUSSION

The MSC/NASTRAN finite element model used in the first phase of the encapsulation program to predict solar cell temperature stress is shown in Figure 1.

The model consisted of rectangular plate elements which simulated the structural panel, the pottant, the cell, and other layers such as front or back covers. As shown in Figure 1, only half of a cell was modelled. Symmetric boundary conditions were imposed along the plane through the cut edge of the cell, and free-edge conditions were imposed along the plane between adjacent cells. In other words, the model behaves as a cantilever beam with the left-hand edge considered fixed and non-rotating.

The boundary conditions imposed on the model permitted the cell and the structural panel to interact as a function of their respective thermal stiffnesses,  $E\alpha$ , where  $E$  is the modulus of elasticity and  $\alpha$  is the coefficient of thermal expansion. The interaction resulted in bending and stretching of the cross-section, as shown in Figure 2. In the figure, shear deformation of the elastomeric pottant is clearly shown.

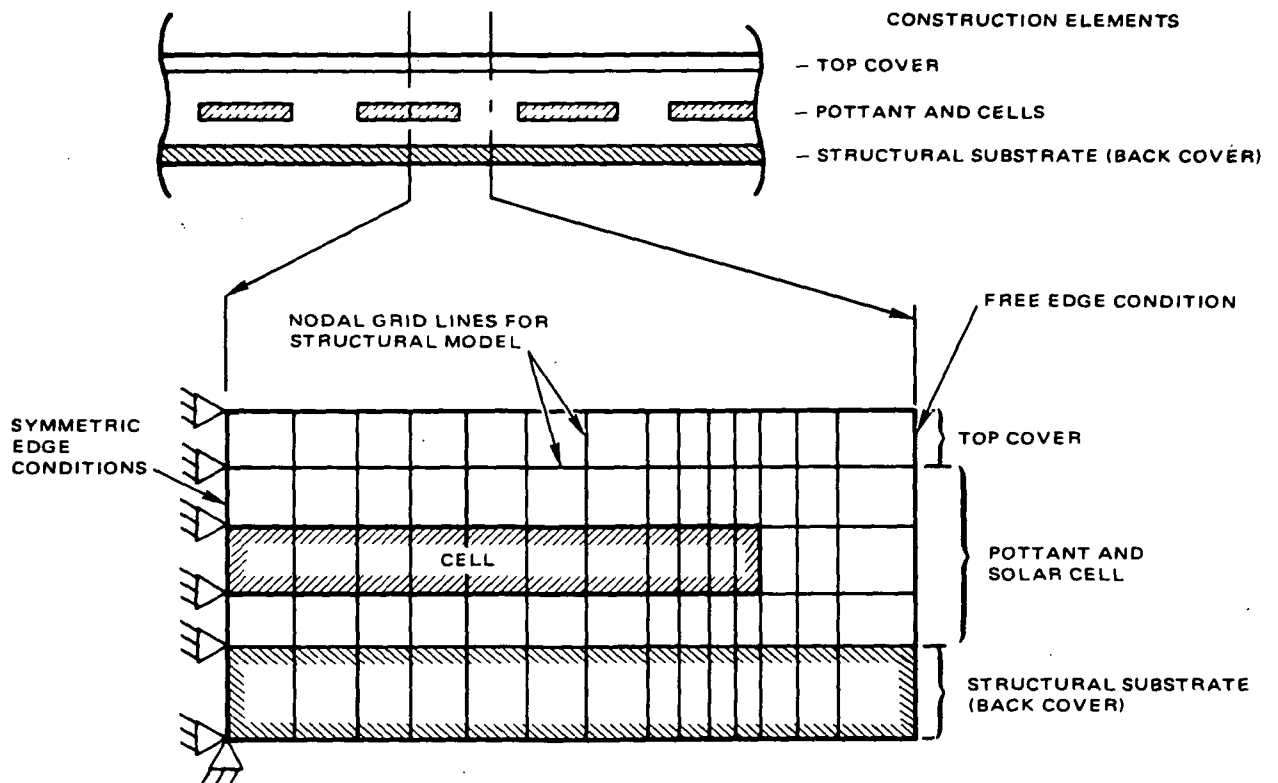


Figure 1. Finite-element structural model for determination of stresses in module construction elements in vicinity of a centrally located cell.

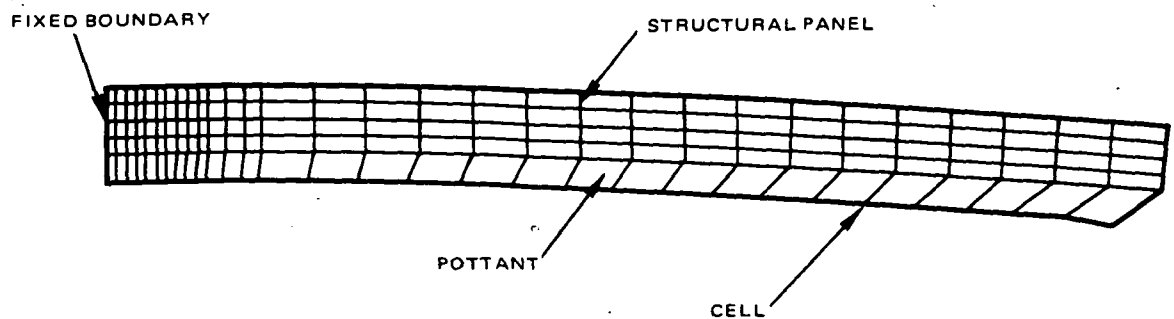


Figure 2. Deflection of structural panel, pottant and cell for 100°C temperature excursion.



The out-of-plane bending capability was provided to enable deformation consistent with that of a classical bimetallic plate when subjected to a uniform temperature change. A bimetallic plate consists of two layers of materials which are bonded together and which have different coefficients of thermal expansion and elastic moduli. Such a plate bends out-of-plane when it undergoes a uniform temperature change (Reference 3). In the case of a photovoltaic module, the two layers are the solar cell and the structural panel, bonded together by the pottant.

The photovoltaic module differs from a classical bimetallic plate since the solar cell layer is not continuous, but instead consists of relatively small tiles. As a result, the temperature-induced loads in the cell are continuous only within the region of each cell. The temperature-induced loads in the structural panel, however, are continuous over the entire module surface. It is expected, therefore, that the out-of-plane bending of a photovoltaic module will be less than that of a classical bimetallic plate. Since out-of-plane bending was expected to reduce solar cell stress, analysis was undertaken to determine solar cell stress when out-of-plane bending is not permitted.

#### SOLAR CELL STRESS WITHOUT MODULE BENDING

A solution for temperature stresses in isotropic laminated plates bonded together by flexible adhesives was derived by L.W. Butterworth and R.K. Yasui of JPL (Reference 4), and is presented in Reference 5. The analysis model is shown in Figure 3.

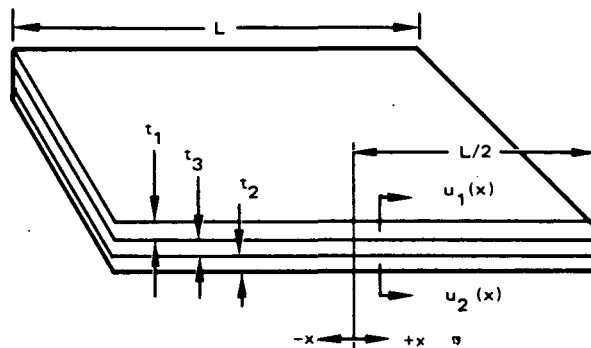


Figure 3. Model of three laminated layers.

It was assumed that the adhesive (pottant) layer had shear stiffness but no axial stiffness. The basic equilibrium equations equate the change in axial stress,  $\sigma_i$ , in each of the outer layers to the shear stress,  $\tau$ , in the bond layer. In the figure  $x$  is the distance from the center of the joint, and the subscripts 1, 2, and 3 refer to the respective layers (in our case, the solar cell, structural panel and pottant). The solutions for axial stress in the outer layers, and shear stress in the adhesive, are given by the following equations:

$$\sigma_1 = \frac{E_1 \Delta \alpha \Delta T}{1 + m n} \left( 1 - \frac{\cosh 2\beta x}{\cosh \beta L} \right) \quad (1)$$

$$\sigma_2 = -m\sigma_1 \quad (2)$$

$$\tau = \frac{2E_1 t_1 \Delta \alpha \Delta T}{1 + m n} \left( \frac{\beta L \sinh 2\beta x}{\cosh \beta L} \right) \quad (3)$$

where

$\sigma_1$  = solar cell axial stress

$\sigma_2$  = structural panel axial stress

$\tau$  = pottant shear stress

$t_1$  = solar cell thickness

$t_2$  = structural panel thickness

$E_1$  = solar cell elastic modulus

$E_2$  = structural panel elastic modulus

$m = t_1 / t_2$

$n = E_1 / E_2$

$L$  = solar cell length

$\Delta \alpha$  = difference between the coefficients of thermal expansion of the solar cell and the structural panel

$\Delta T$  = change in temperature  
= cell temperature - ambient temperature

cosh = hyperbolic cosine function

sinh = hyperbolic sine function

The dimensionless term  $\beta L$  is a measure of the relative stiffness of the cell, the structural panel, and the pottant, where

$$\beta^2 = \frac{1}{4} \frac{G_3}{t_3} \left( \frac{1}{E_1 t_1} + \frac{1}{E_2 t_2} \right)$$

$G_3$  = pottant shear stiffness

$t_3$  = pottant thickness

For flexible pottants typical of photovoltaic module construction,  $\beta L \leq 4$ . If the pottant is very stiff (i.e., high modulus and/or small thickness),  $\beta L$  is large.

Solar cell and pottant stresses for a typical module construction were computed as a function of pottant thickness and are compared to the results of the previous with-bending analyses in the next section.

## RESULTS

Solar cell stress was computed for EVA pottant ( $E = 1000$  psi), a 4 in.  $\times$  4 in.  $\times$  0.01 in. silicon solar cell, and glass, wood, and steel structural panels. The results are plotted in Figures 4, 5, and 6.

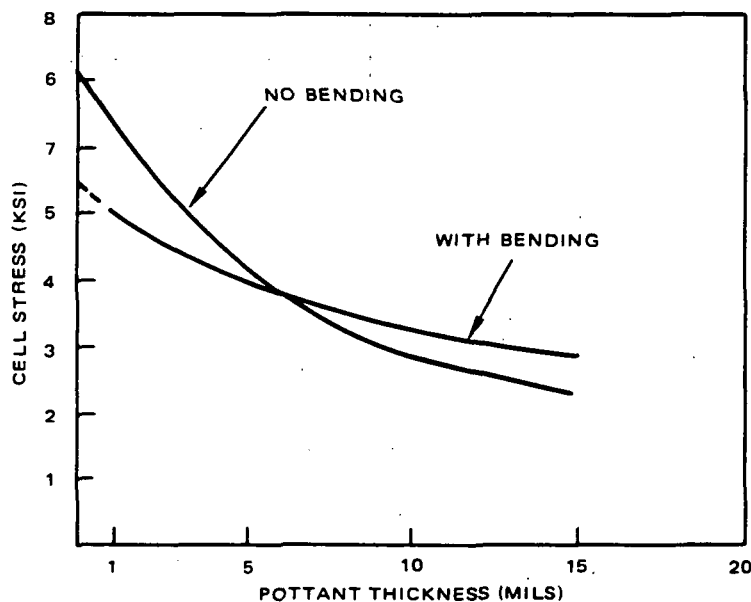


Figure 4. Cell stress for a glass structural panel, EVA pottant,  $\Delta T = 100^\circ\text{C}$ , 4 in.  $\times$  4 in.  $\times$  0.01 in. silicon cell.

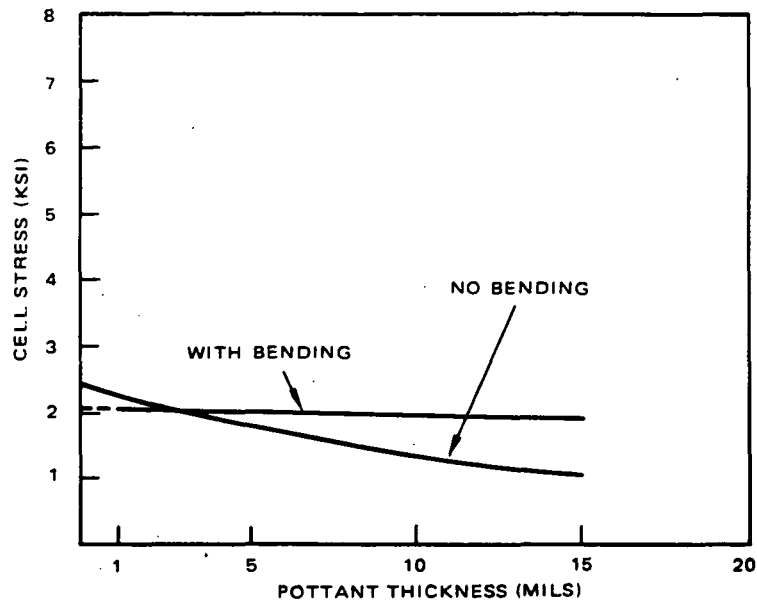


Figure 5. Cell stress for a wood structural panel, EVA pottant,  $\Delta T = 100^{\circ}\text{C}$ , 4 in. x 4 in. x 0.01 in. silicon cell.

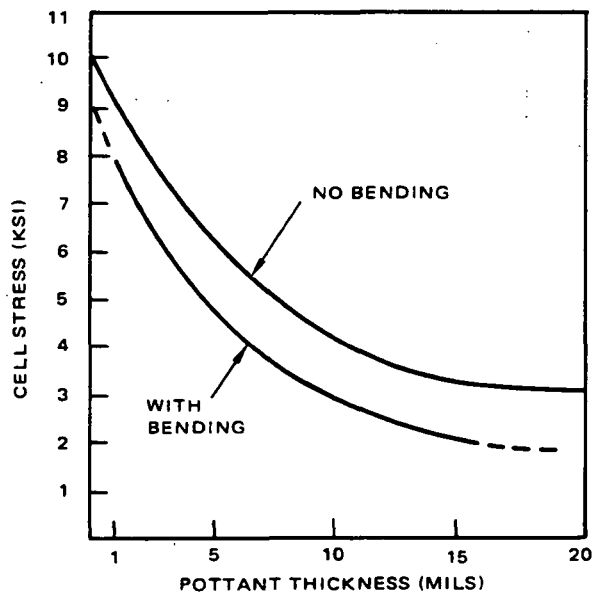


Figure 6. Cell stress for steel structural panel, EVA pottant,  $\Delta T = 100^{\circ}\text{C}$ , 4 in. x 4 in. x 0.01 in. silicon cell.

Figure 4 is a plot of solar cell stress for a glass structural panel. For pottant thicknesses less than 1 mil, the solar cell stress is approximately 25 percent higher when bending is not permitted, which was expected. For pottant thicknesses greater than about 6 mils, the cell stress is higher when bending is permitted. This is probably due to the effect of the offset of the solar cell from the neutral axis of the laminate. As the pottant thickness increases, the offset bending influence becomes more significant. For a pottant thickness of 15 mils, the cell stress is approximately 25 percent higher when bending is permitted.

Similar trends are seen in Figure 5 which is a plot of solar cell stress for a wood structural panel. For pottant thicknesses less than 1 mil, the cell stress is about 25 percent higher when bending is not permitted. For pottant thicknesses greater than about 3 mils, the cell stress is higher when bending is permitted. For a pottant thickness of 15 mils, the cell stress is approximately 50 percent higher when bending is permitted.

Figure 6 is a plot of cell stress for a steel structural panel. In this case, the cell stress is always higher when bending is not permitted. For small values of pottant thickness, the cell stress is about 10 percent higher when bending is not permitted. The difference increases as the pottant thickness increases. For a thickness of 15 mils, the cell stress is about 70 percent higher when bending is not permitted.

A possible cause for the difference between the results for the steel panel and those for the glass and wood panels is the thickness of the panels. The steel panel ( $t = 0.08$  in) is much thinner than either the glass panel ( $t = 0.125$  in) or the wood panel ( $t = 0.25$  in). The smaller thickness of the steel panel probably reduces the significance of the bending behavior.

Figure 7 is a plot of the pottant shear stress for glass, wood, and steel structural panels when bending is not permitted. These stresses were computed using Equation 3. Finite element predictions of pottant shear stress are not available. The allowable pottant shear stress is 100 psi, shown by the dotted line. It is seen that pottant shear stress is highest for steel and lowest for wood. The allowable shear stress of 100 psi is exceeded for pottant thicknesses less than 3 mils for a steel panel, and pottant thicknesses less than 2 mils for a glass panel. Pottant shear stress is always less than the allowable for a wood panel. It should be noted that the pottant shear stress is zero at the center of the cell and highest at the edge of the cell.

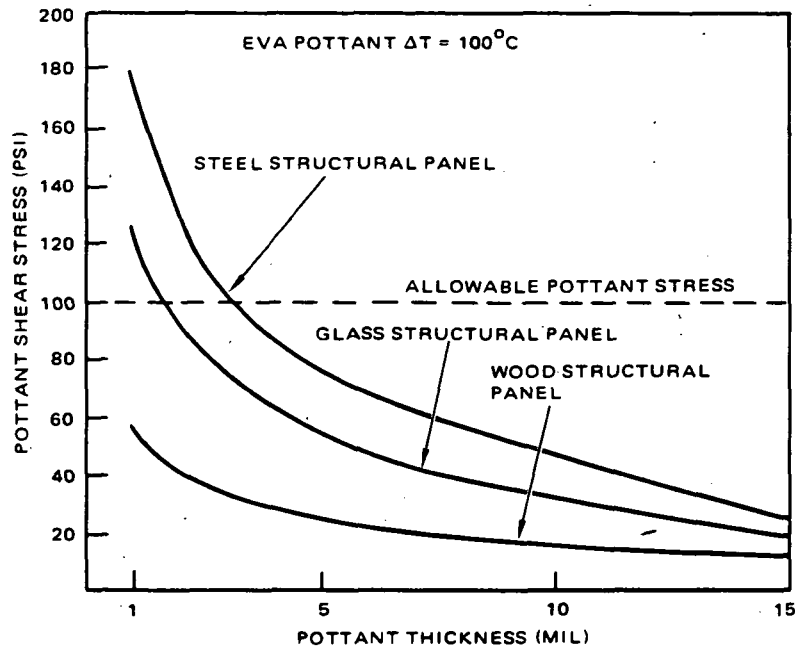


Figure 7. Pottant shear stress (bending not permitted).

## ADDITIONAL CONSIDERATIONS

### 1. Solar Cell Length

In equation 1, it can be seen that as  $\beta L$  is increased, the cell stress approaches an upper bound given by

$$\sigma_1 = \frac{E_1 \Delta \alpha \Delta T}{1 + mn}$$

On the other hand, in the previously derived master curve for cell temperature stress (shown in Figure 8) it is seen that the cell stress increases as  $L_C^{1.5}$ , where  $L_C$  is the cell length. The finite element analyses from which the master curve was generated did not consider cells greater than 4 inches in length. Therefore, the master curve should not be used for cell lengths greater than 4 inches until additional analyses are performed to verify or modify the master curve cell length parameter. It should be noted that both the no-bending solution and the with-bending solutions predict that the cell stress decreases as cell length is decreased.

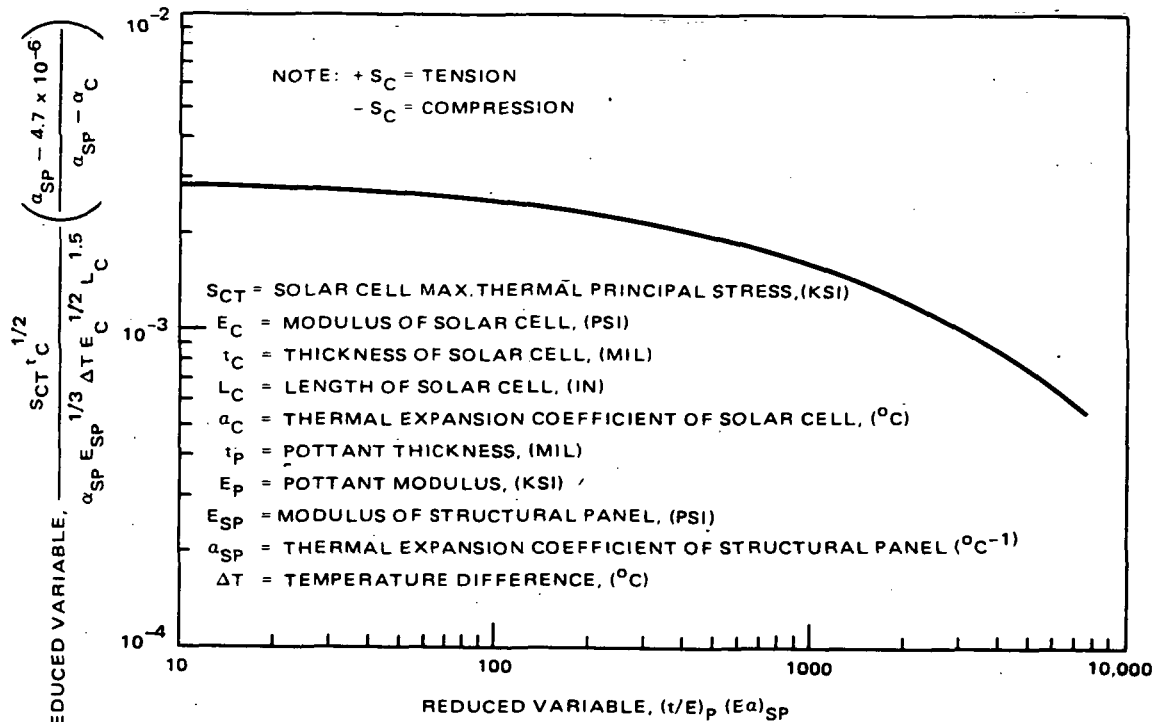
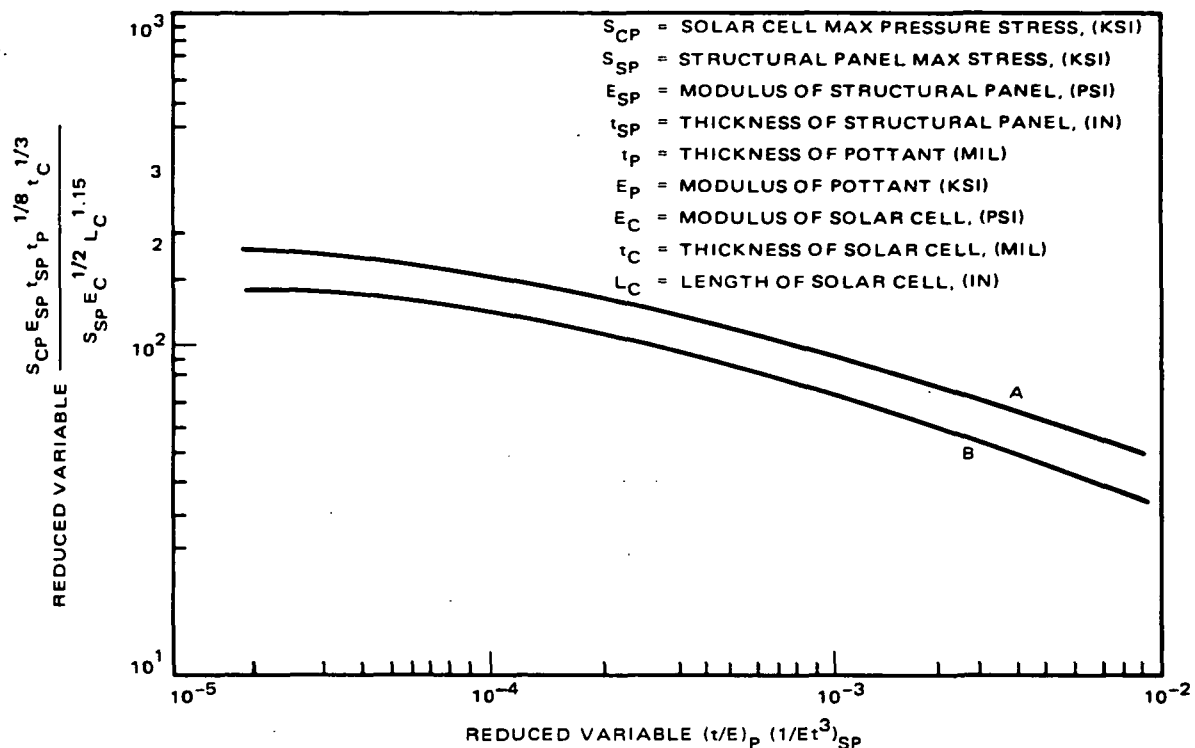


Figure 8. Master curve for thermal stress analysis.

## 2. Biaxial Material Properties

The master curves for thermal stress analysis (Figure 8) and pressure stress analysis (Figure 9) are generalized for the elastic moduli of the solar cell, the pottant, and the structural panel. If the cell is long and narrow (i.e., beam-like), the ordinary elastic moduli,  $E_i$ , of the layers should be input to the master curves to compute cell stress. However, if the cell is a rectangular plate, or is circular, the quantity  $E_i / (1 - \nu_i)$  should be used, where  $\nu_i$  is Poisson's ratio of layer 'i.' This is due to the effective stiffening of a biaxially stressed plate by the Poisson's ratio effect.



NOTE: USE CURVE A FOR PRESSURE  $\leq 10$  PSF. USE CURVE B FOR PRESSURE = 50 PSF. FOR INTERMEDIATE LOADS, INTERPOLATE LINEARLY BETWEEN A AND B.

Figure 9. Master curve for pressure stress analysis.

## ACKNOWLEDGEMENTS

The author is grateful to the following individuals for the many helpful suggestions which aided the development of this work: R.E. Holman, I.R. Jones, and J.M. Kallis of Hughes Aircraft Company, E.F. Cuddihy, C.D. Coulbert, and R.G. Ross of The Jet Propulsion Laboratory, and A. Garcia of Spectrolab, Inc.

## REFERENCES

1. Hughes Aircraft Co., "Design, Analysis, and Test Verification of Advanced Encapsulation System—Phase 1 Interim Report," Spectrolab Letter Contract #9PMY2636321/88774.
2. Duncan, L.B., "Structural Analysis," Hughes Aircraft Company Report, Spectrolab Letter Contract #79PMY2636321/88774, June 1983.
3. Roark, R.J. and Young, W.C., "Formulas for Stress and Strain," McGraw Hill Book Company, Fifth Edition, 1975.
4. Butterworth, L.W., and Yasui, R.K., "Structural Analysis of Silicon Solar Arrays," Report No. 32-1528, Jet Propulsion Laboratory, May 1971.
5. Rauschenbach, H.S., "Solar Cell Array Design Handbook," Van Nostrand Reinhold Company, 1980.